Chapter 5

Fabrication of Nano-heterostructured Composites of $Ag/Ag_2O/ZnO$ by $-SO_3H$ Functionalized Organic Salts for Photocatalytic Study of Organic Dyes

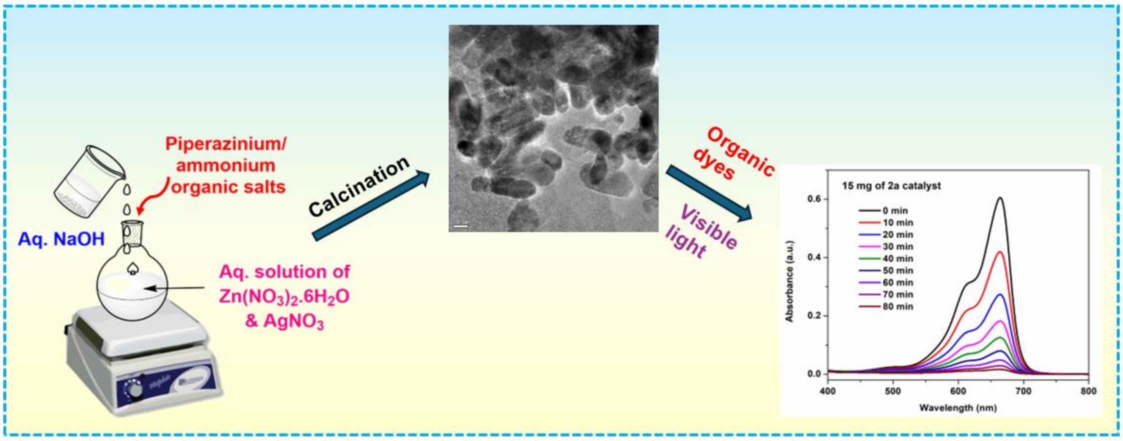

Synopsis

In this work, two Ag/Ag_2O integrated heterostructured ZnO nanocomposites (**2a** & **2b**) were fabricated using aqueous solution of two Brønsted acidic organic salts i.e. 1,4-disulfopiperazine-1,4-diium chloride ([DSPZ].2Cl]) and 2-methyl-1,3-disulfoimidazolium chloride ([MDSIM]Cl) under heating conditions. The structures of **2a** & **2b**, with varied size of nanoparticles, were confirmed by using analytical results of PXRD, SEM, EDX, Raman, UV-Vis DRS, TEM, XPS, BET etc. Photocatalytic efficiencies of both the composites were explored in degradation of model dye methylene blue (MB), where nearly complete degradation was obtained under the optimized dose of catalysts in basic medium (pH=10), contrary to the lesser degradation at lower pH. In the degradation of mixed dyes of methyl orange (MO)-methylene blue (MB), better degradation was observed for MO in all the pH studied than that for MB dye. The splendid photocatalytic performances of the Ag/Ag_2O/ZnO nanocomposites in the degradation of dye molecules studied could be attributed to the synergistic effects of Ag, Ag_2O and ZnO nanophases within the interface structures, which resulted in an effective charge separation for lowering of electron-hole recombination rate. The photocatalyst (**2a**) also exhibited recyclability for 4 consecutive runs with a slight decrease in its degradation efficiency gradually.

5.1. Introduction

Heterostructures are nanomaterials composed of two or more semiconductor substances with specific compositions, having interface in their heterojunctions with unequal bandgaps [1, 2]. Their properties can be tuned through variation of semiconductor materials in the interfaces with desired functionalities. Depending on the arrangements and interfaces of the heterostructures, they would exist in spherical (0D), cylindrical (1D), planar (2D) and cubic (3D) nanocomposites with unique properties and performances. Therefore, in material science, the designing of heterostructures have received significant importance because of their versatile optical and electronic properties for potential uses as photocatalysts, memory devices, photodetectors and optoelectronic devices etc [3]. Furthermore, these nanocomposites exhibit greater characteristics due to the synergistic interactive effects of all the components than the individual semiconductor components. Most common methods to fabricate the nano heterostructures include co-precipitation, solid state reaction, sol-gel, pyrolysis, hydrothermal/solvothermal methods [4, 5]. Some of these methods require high pressure and temperature reaction vessel along with more preparation time. These limitations could be reduced as benign routes involving microwave energy [6], ultrasonic energy [7, 8], photochemical energy [9], bio-assisted and ionic liquid assisted [8, 10] procedures.

For the development of metal oxide nanocomposites, ZnO is a promising [10-12] eco-friendly and cost-efficient n-type semiconductor with high thermal/electrochemical stability and wide band gap (3.3 eV) that offers photo-response only to shorter wavelength region [13, 14]. Therefore, the inefficient separation of photogenerated electron/hole pairs in ZnO causes rapid recombination the pairs and restricts maximum utilization of light during the photocatalytic reactions of ZnO [15, 16]. Additional drawbacks related to the ZnO NPs as semiconductor include corrosion, deactivation, agglomeration, difficulty in reuse etc. [17].

The construction of ZnO nanocomposites with small quantities of noble metals (Ag, Au or Pt) or their oxides reported to lower the electron-hole recombination rate of the ZnO nano heterostructures along with the modification of other properties [18-20]. These nanomaterials displayed broadening of photo responsive region to visible range that increased the photocatalytic activity to decompose organic pollutants like dyes, antibiotics, pesticides etc. [21]. Considering the low cost and easy availability of the Ag metal as compared to the Au or Pt metals, numerous studies on the synthetic routes, following the earlier mentioned methods [4, 5], and photocatalytic behaviour of Ag based ZnO nanocomposites are found [22, 23].

In this case, the ionic liquid-assisted NPs synthesis represents a benign route in terms of its capacities to develop tuned structures of NPs with variable optical and electronic properties by acting as solvent, template or by providing stabilizing effects. Since, with the diversified cation-anion combinations of ionic liquids, they change the physicochemical properties of ILs which may involve various inter/intra molecular interactions during the nanoparticle synthesis [22]. It was found that they reduce the tendency of metal NPs to cause agglomeration with their stabilizing effects. By modifying the sizes of organic cations and anions of the ionic liquids, controlled growth of the metal NPs with distinct morphologies was achieved in a simple way [24]. For example, the sizes of Cr, Mo and W metal NPs synthesized from precursor metal carbonyls in imidazolium-based ILs with anions of different sizes displayed large sized NPs formed with bigger volume anions such as $[(CF_3SO_2)_2N]^-$ as compared to relatively smaller $[CF_3SO_3]^-$ and $[BF_4]^-$ anions [25]. For the fabrication of Ag based ZnO NPs in ionic liquids, few reports were observed in the literature using wet chemical, photochemical as well as ultrasonic methods [10, 26, 27], which are mentioned in **Chapter 1, unit 1A.6**. They worked either as template, solvent, stabilizer or capping agent during formation of the Ag based ZnO nanocomposites.

Based on the above literature survey, it was aimed to fabricate two samples of Ag based ZnO nanocomposites (**Scheme 5.1**) in aqueous solution of sulfonic acid functionalized Brønsted acidic organic salts, namely 1,4-disulfopiperazine-1,4-diium chloride ([DSPZ].2Cl]) and 2-methyl-1,3-disulfoimidazolium chloride ([MDSIM]Cl), respectively, as stabilizing agents for controlled growth of the Ag based ZnO nanocomposites by precipitation method in aqueous medium in an environment of strong intra/inter-molecular H-bonding interactions [28, 29]. After that, their efficacy as photocatalysts were evaluated for the degradation of representative cationic dye methylene blue (MB) and its mixtures with anionic dye methyl orange (MO) as well as another cationic dye crystal violet (CV) in neutral, acidic and basic conditions at ambient temperature. It is known that the exposure of such synthetic dyes to nature in large amounts can cause serious environmental issues like difficulty in waste management, contamination of water/soil etc., which can lead to many health hazards in living systems [30, 31]. Hence, degradation of the organic pollutants/dyes to ecologically harmless compounds, using simple recyclable heterogeneous photocatalysts, hold immense significance as compared to using conventional water treatment methods, as most of the common methods of wastewater treatments suffer from problems like involvement of costly reagents/auxiliaries, secondary pollution such as large amounts of sludge generation, deterioration in water quality, restricted application etc. [32, 33].

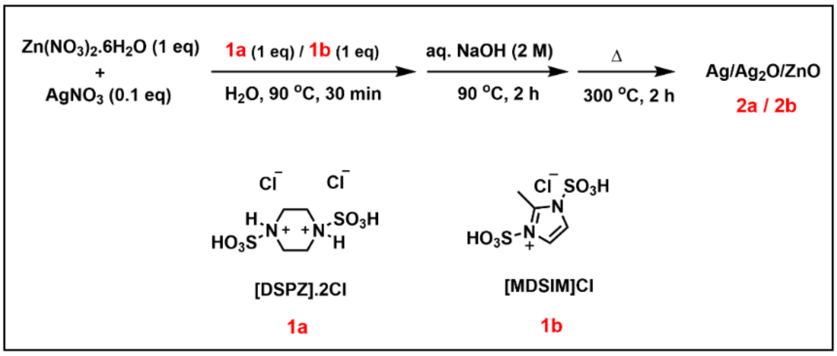

Scheme 5.1: Synthesis of $Ag/Ag_2O/ZnO$ nanocomposites (**2a** and **2b**).

5.2. Results and discussion

5.2.1. Characterization of Ag/Ag_2O/ZnO nanocomposites

Firstly, two Ag/Ag_2O/ZnO nanocomposites (**2a** & **2b**) were prepared from aqueous solutions of $Zn(NO_3)_2.6H_2O$ and $AgNO_3$, assisted by two organic salts [DSPZ].2Cl and [MDSIM]Cl, *via* precipitation method according to **Scheme 5.1**. The structural compositions of the nanoheterostructures were confirmed by PXRD, SEM, EDX, Raman, UV-Vis DRS, TEM, XPS, BET etc. techniques. The photocatalytic efficacies of the synthesized nanocomposites were checked in the degradation of organic dyes under visible light (MB, MB+MO, MB+CV).

5.2.1.1. FT-IR spectroscopy analysis

The FT-IR spectra of **2a** and **2b** nanomaterials showed several peaks in functional group and fingerprint regions (**Fig. 5.1**). The peaks around 1628-1626 cm^{-1} along with broad peaks at 3415 cm^{-1} in **2a** and **2b** occurred due to O-H bending and stretching vibrations of adsorbed water molecules of nanomaterials, respectively [34, 35]. While peaks around 2925-2924 cm^{-1} and 1424-1422 cm^{-1} were attributed to stretching and bending vibrations of C-H bond of $-CH_3$ or $-CH_2$ groups present in parent organic salts [29], the sharp peaks at 1123-1118 cm^{-1} were assigned to symmetric stretch of S-O bond of $-SO_3H$ groups [36]. Stretching vibration for Ag-O-Ag bond in Ag_2O was represented by the peaks around 619-617 cm^{-1} [37]. The peaks around 431-421 cm^{-1} could be attributed to Raman active E2 stretching vibrational mode of hexagonal ZnO nanoparticles [38, 39, 40], whereas the peaks at 544-511 cm^{-1} might be connected to oxygen-deficiency in ZnO lattices [38]. FT-IR spectrum of **2b** possessed additional absorptions in the functional-group region as compared to the spectrum of **2a**.

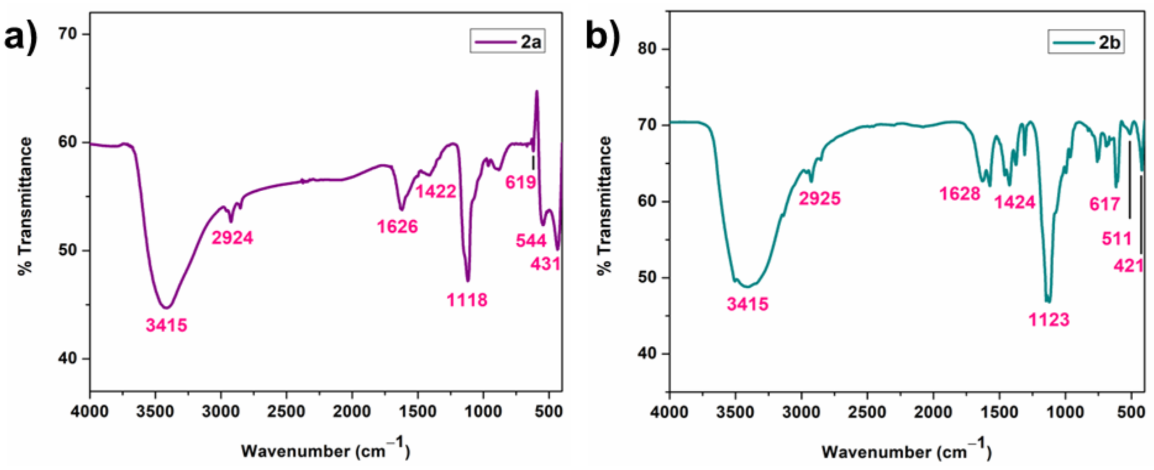

Fig. 5.1: FT-IR spectra of a) **2a** and b) **2b** nanomaterials.

5.2.1.2. Scanning Electron Microscopy analysis

The SEM images of **2a** and **2b** materials were shown in **Fig. 5.2a** and **5.2b**, respectively. From the images with a microscopic resolution of 200 nm, it was observed that both **2a** and **2b** materials possessed crystalline granules of different shapes and sizes. The granules of **2a** were capsule-like with slight varying shapes, while those of **2b** exhibited irregular sheet-like structures and sizes. The agglomeration of granules was noted in both cases. The surface morphology of **2a** seemed to be more homogeneous than the surface of **2b** due to more clustering of the sheet-like structures in the latter.

5.2.1.3. Energy Dispersive X-ray analysis

EDX images of **2a** and **2b** materials were shown in **Fig. 5.3a** and **Fig. 5.4a**, respectivey, which verified the presence of all preferred elements in both the materials. In case of **2a**, the studied area contained nearly equal atomic% of Zn and O (**Fig. 5.3a inset**). **Fig. 5.3b-e** and **Fig. 5.4b-e** displayed the mapping images of combined as well as individual elements overlaying the material surfaces. As expected, less abundance of Ag were observed for both the nanomaterials as compared to the other two elements.

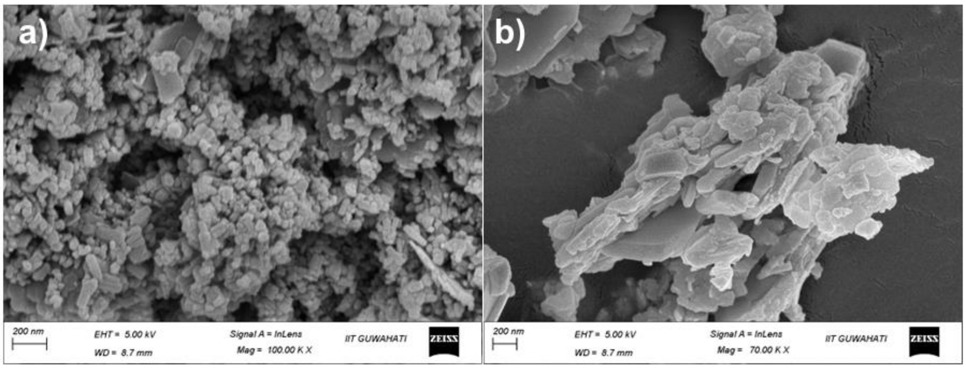

Fig. 5.2: SEM images of materials a) **2a**, b) **2b**.

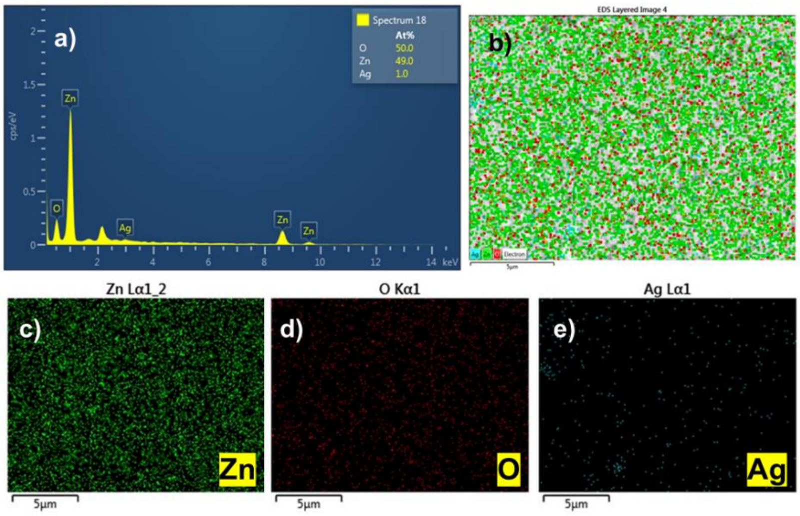

Fig. 5.3: a) EDX image of **2a** (atomic% of elements in inset), b-e) elemental mapping images of all the constituent atoms of **2a** material.

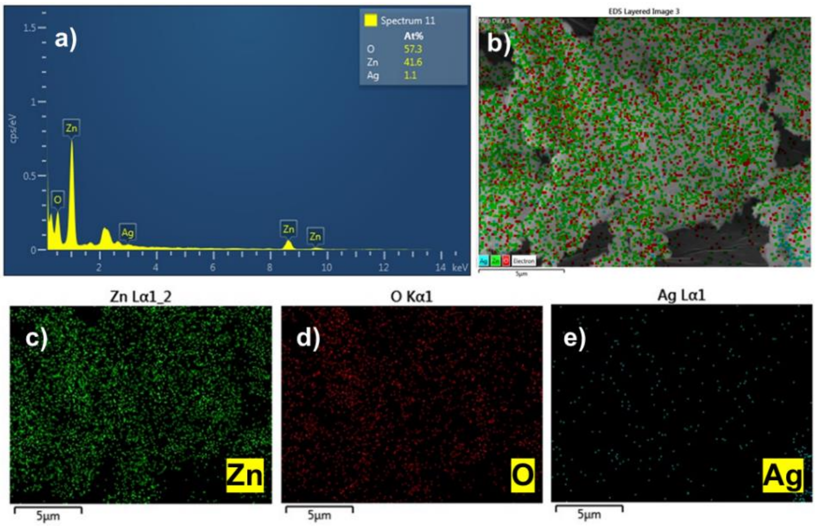

Fig. 5.4: a) EDX image of **2b** (atomic% of elements in inset), b-e) elemental mapping images of all the constituent atoms of **2b** material.

5.2.1.4. Powder X-ray Diffraction analysis

The powder X-ray diffraction patterns for **2a** and **2b** materials showed characteristic diffraction peaks for all the constituent elements in their metallic and/or oxide forms. In the case of **2a** (**Fig. 5.5a**), the peak at 36.25° was aligned with the most intense peak of ZnO, according to JCPDS card no. 36-1451 and represented (101) reflection plane of hexagonal primitive crystal lattice of ZnO in Wurtzite-type structure [41, 42]. The other peaks of 2**a** positioned at 31.77°, 34.42°, 47.53°, 56.60°, 62.86°, 66.38°, 67.96°, 69.10°, 72.56° and 76.95° could be assigned for (100), (002), (102), (110), (103), (200), (112), (201), (004) and (202) reflection planes of ZnO, respectively. As per JCPDS card no. 65-6811 [43, 44], the 2θ peaks at 32.22°, 38.10°, 46.22°, 54.84° and 57.50° could be allotted to crystalline planes (111), (200), (211), (220) and (221) of cubic Ag_2O primitive lattice, respectively. In addition, the only reflection plane (200) of cubic face-centered lattice (fcc) of Ag at 38.10° (JCPDS card no. 04-0783) overlapped with that of Ag_2O [45, 44]. Most of these diffractive peaks for **2a** were also displayed by **2b** material (**Fig. 5.5b**). However, subtle changes in intensity and 2θ positions of some peaks were noticed while comparing the two materials, which could be accounted for different stabilizing effects of sulfonic acid-functionalized organic salts for nanoparticle formation in aqueous solution involving network of intra/inter-molecular H-bonding interactions.

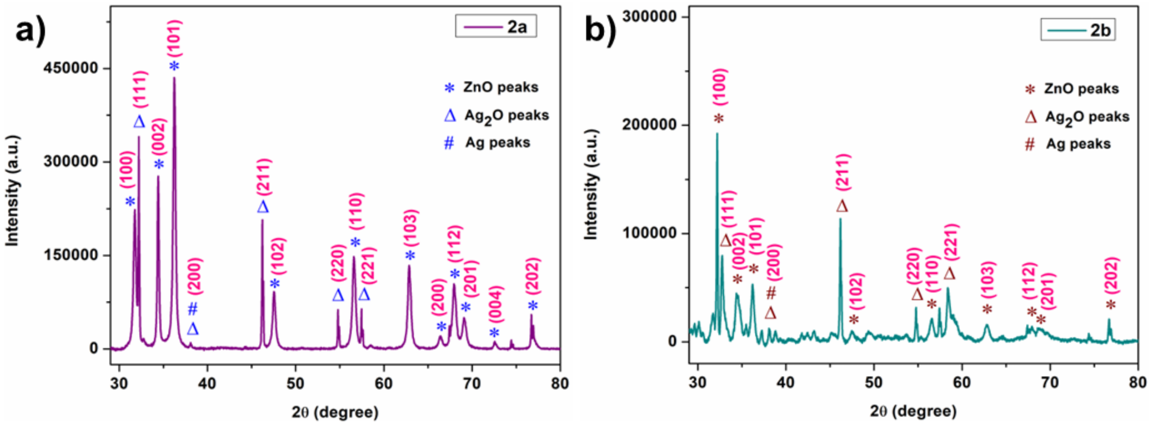

Fig. 5.5: PXRD patterns of **2a** and **2b** materials.

5.2.1.5. BET analysis

The Brunauer-Emmet-Teller (BET) isotherm plots of **2a** and **2b** materials for N_2 gas adsorption-desorption gave information about their specific surface area, pore volume and pore diameter (**Fig. 5.6**). Both the materials exhibited typical type IV isotherms with hysteresis loop of capillary condensation, indicating mesoporous nature of the materials [46, 18]. The specific surface area for material **2b** was found to be slightly larger (26.5 m^2/g) than that of 2a (20.2 m^2/g). However, the pore volume of both materials was almost similar, precisely 0.045 cc/g for 2a and 0.047 cc/g for **2b** material. **Fig. 5.6 (inset)** also depicted Barrett-Joyner-Halenda (BJH) curves to showcase the pore-size distribution over both the **2a** and **2b** material surfaces, where ~2-15 nm was observed to be the prime range for the materials. Both the **2a** and **2b** composites possess pore diameter of 2.381 nm and 3.860 nm respectively, as seen from the BJH plots of the materials.

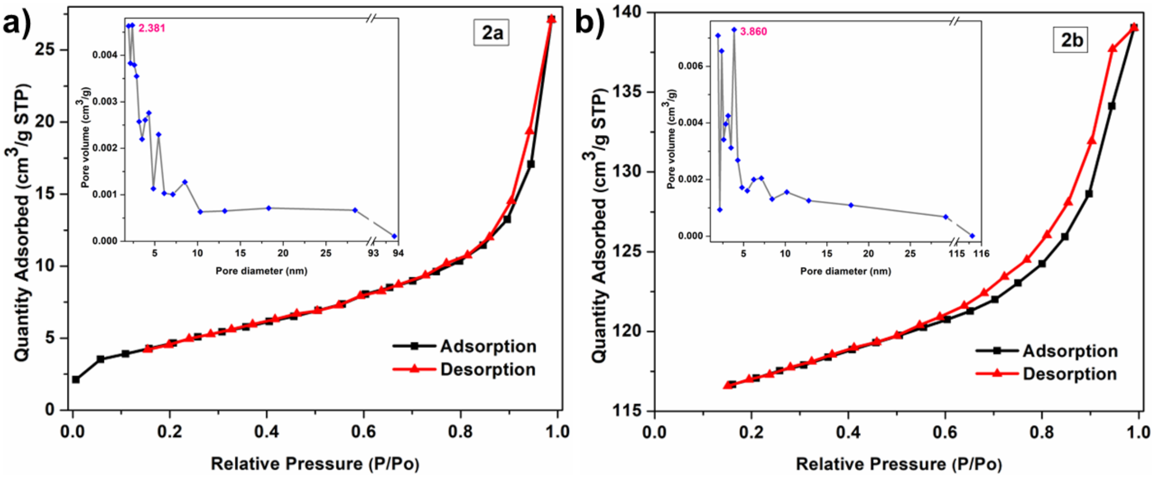

Fig. 5.6: BET isotherm and BJH plot of a) **2a**, and b) **2b** materials (BJH plots of the materials were shown in the inset).

5.2.1.6. Transmission Electron Microscopy analysis

The TEM analyses of **2a** and **2b** were carried out to have a better understanding of morphology as well as appearance of the nano materials (**Fig. 5.7 and 5.8**). **Fig. 5.7a-b** clearly displayed the ZnO nano capsules, as revealed by SEM images (**Fig. 5.2a**) having an average size of 59.7 nm (**Fig. 5.7c**) along with Ag nanoparticles (average size of 27.56 nm, **Fig. 5.7d**) positioned at one end of the ZnO capsules like a cap. The spacing calculated from lattice fringes was found to be 0.191 nm (**Fig. 5.7e**), which supported the d-spacing referring to the (102) plane of wurtzite ZnO. The selected area electron diffraction (SAED) pattern for **2a** portrayed distinct diffraction planes (**Fig. 5.7f**) which were in accordance with those obtained from the PXRD analysis. **Fig. 5.8a-b** revealed nearly round-shaped ZnO nanosheets with an average size of 191.17 nm for **2b** nanomaterial (**Fig. 5.8c**) along with the scattered Ag nanoparticles (average size 22.34 nm, **Fig. 5.8d**). Although the distinct diffraction planes obtained from the SAED pattern for **2b** (**Fig. 5.8f**) could be well-verified with the PXRD reflections, spacing calculation from the lattice fringes was unachievable due to the obscure lattice fringes in **2b** (**Fig. 5.8e**). These images further substantiate the formation of desired ZnO-Ag nanocomposites, which contained meso-ranged pores as described in the BET analysis of the materials (**Fig. 5.6**).

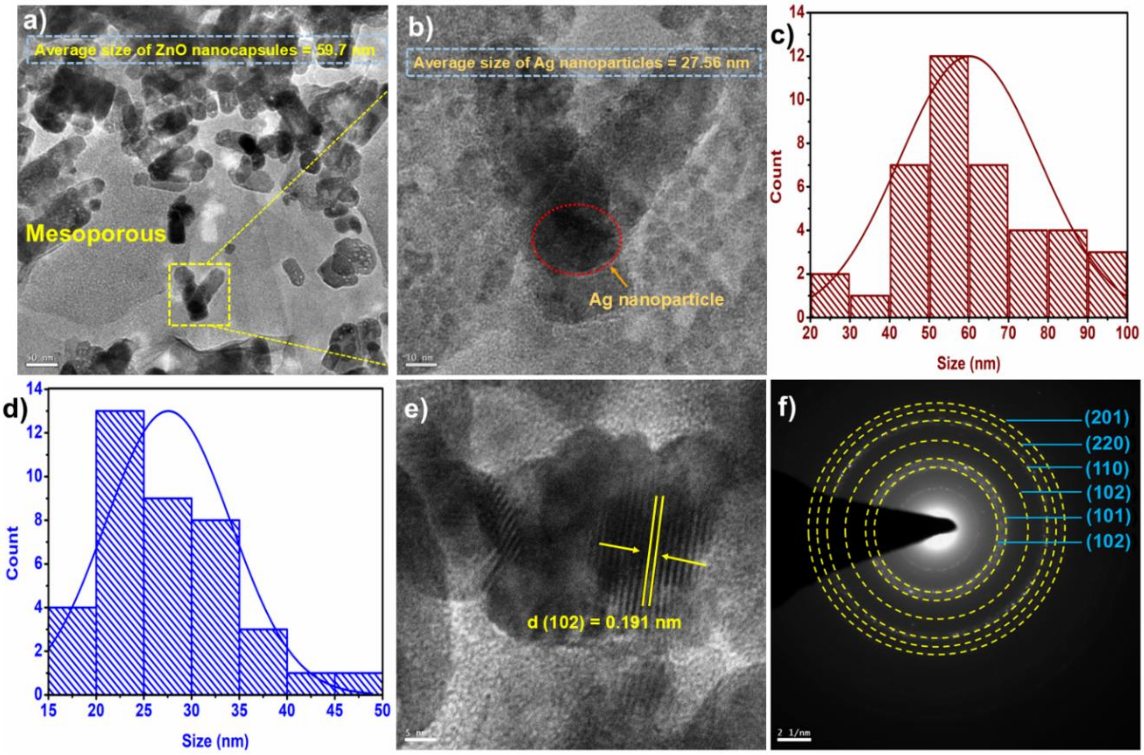

Fig. 5.7: a) Lower magnified TEM image of **2a** along with size distribution of ZnO nanocrystals, b) Higher-magnified TEM image of **2a** along with size distribution of Ag nanoparticles, c) ZnO nanocapsule size histogram, d) Ag particle size histogram, e) Lattice fringes of **2a**, f) SAED pattern for **2a**.

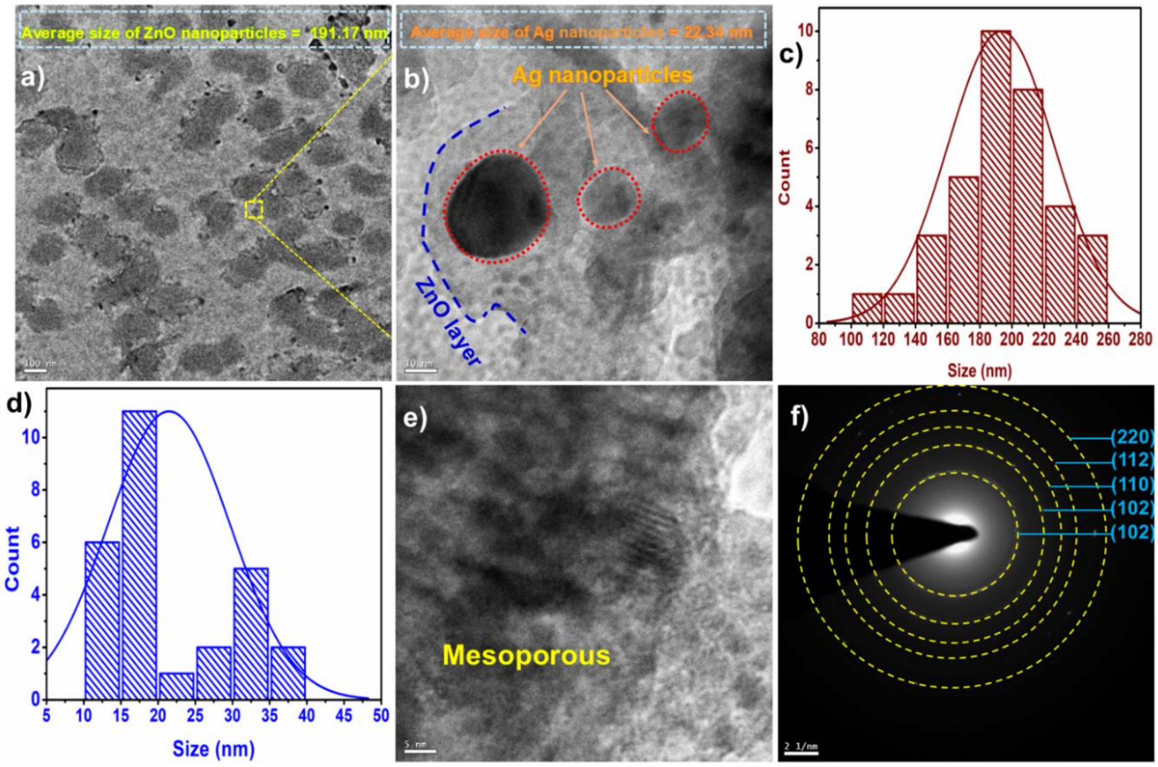

Fig. 5.8: a) Lower magnified TEM image of **2b** along with size distribution of ZnO nanocrystals, b) Higher-magnified TEM image of **2b** along with size distribution of Ag nanoparticles, c) ZnO nanolayer size histogram, d) Ag particle size histogram, e) Lattice fringes of **2b**, f) SAED pattern for **2b**.

5.2.1.7. Raman analysis

Raman spectra of **2a** and **2b** nano materials were given in **Fig. 5.9**, where change in Raman shifts and intensity of peaks was observed for the materials. The wurtzite crystal of ZnO in **2a** and **2b**, as identified from the PXRD patterns (**Fig. 5.5**), provided optical phonons at Γ point by $\Gamma_{opt} = 1A_1 + 2B_1 + 1E_1 + 2E_2$ [41, 47, 48]. The polar modes A_1 and E_1 were divided into two optical modes, namely transverse optical (TO) and longitudinal optical (LO). $E_2^{(high)}$ and $E_2^{(low)}$ modes were the two frequency phonon modes of E_2, where $E_2^{(low)}$ was linked to sublattices of Zn metals and $E_2^{(low)}$ followed oxygen atomic vibrations. However, $B_1^{(high)}$ and $B_1^{(low)}$ modes were found to be Raman inactive. The distinctive Raman active A_1(TO), $E_2^{(high)}$ and A_1(LO) modes of ZnO were found at 380 cm^{-1}, 441 cm^{-1}, 567 cm^{-1} for the **2a** and 375 cm^{-1}, 423 cm^{-1}, 563 cm^{-1} for the **2b** respectively [39]. The peaks at 496 cm^{-1}, 749 cm^{-1} in **2a** and 754 cm^{-1} in **2b** occurred due to surface optical phonon modes of ZnO, although the former was absent in **2b** [47, 49]. Raman shifts at 133 cm^{-1} in **2a** and 146 cm^{-1} in **2b** were attributed to vibrational mode of Ag lattice, while peaks at 240 cm^{-1}, 995 cm^{-1} in case of **2a** and 257 cm^{-1}, 1006 cm^{-1} in case of **2b** represented the stretching/bending modes of Ag-O bond in Ag$_2$O [50, 37]. In addition, shifts at 1372 cm^{-1}, 1522 cm^{-1} in **2a** and 1361 cm^{-1}, 1525 cm^{-1} in **2b** were related to Ag nanoparticles [39].

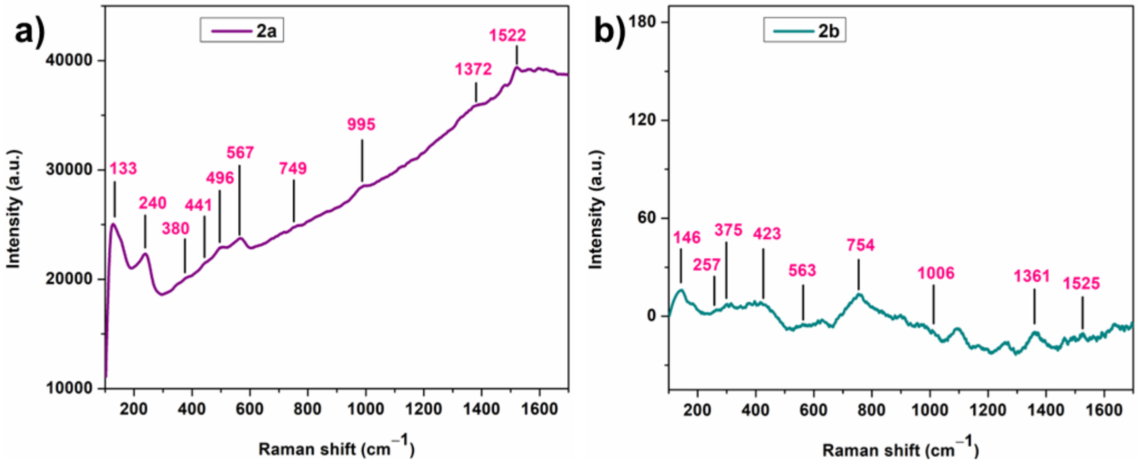

Fig. 5.9: Raman spectra of a) **2a**, and b) **2b** materials.

5.2.1.8. XPS analysis

X-ray photoelectron spectroscopy (XPS) analyses of **2a** and **2b** were carried out to verify the existence of constituent elements and to get information about their chemical status in the nanomaterials (**Fig. 5.10** and **Fig. 5.11**). The elements Zn, Ag and O could be observed in the survey spectra of **2a** in **Fig. 5.10a** [33]. XPS spectrum of Zn 2p gave two peaks at 1044.7 eV and 1021.5 eV, which represented $2p_{1/2}$ and $2p_{3/2}$ states of Zn^{2+} form in ZnO (**Fig. 5.10b**). The Gaussian two-peak fitting of Ag 3d XPS spectrum produced two peaks at 372.6 eV and 366.6 eV, attributing to Ag $3d_{3/2}$ and Ag $3d_{5/2}$ states, respectively (**Fig. 5.10c**). The difference between these two peaks was found to be 6 eV, which was in accordance with the literature [51]. Each of these two peaks gave rise to two components after deconvolution, where the components at 373.2 eV and 367.0 eV denoted the Ag (0) state of Ag metal, while the components at 372.7 eV and 366.7 eV denoted the Ag (+1) oxidation state of Ag$_2$O [52]. By calculating the area covered by these four components of Ag 3d state, it was found that Ag was distributed over the ZnO nanocapsules as Ag metal and Ag$_2$O in nearly equal ratio. **Fig. 5.10d** portrayed Gaussian two-peak fitting of O 1s XPS spectrum at 530.5 eV, where binding energy at 531.6 eV denoted surface oxygen and binding energy at 530.4 eV denoted metal-oxygen [53]. Likewise, chemical status of the constituent elements of **2b** was shown in **Fig. 5.11**. The survey spectra showed the presence of Zn, Ag and O elements in **2b** with their respective states (**Fig. 5.11a**). Nonetheless, slight change in the peak positions in case of all three elements (Zn, Ag and O) in **2b** were observed towards higher binding energy values (**Fig. 5.11b-d**). Additionally, from the calculation of area covered by the components of Ag 3d state in case of **2b** material, Ag was found to be distributed over the ZnO nanosheets as 54% Ag_2O and 46% Ag metal, which slightly contradicted the nearly even formation of Ag and Ag_2O in case of the **2a** sample. Overall, both the synthesized materials could be assigned as $Ag/Ag_2O/ZnO$ nanomaterials.

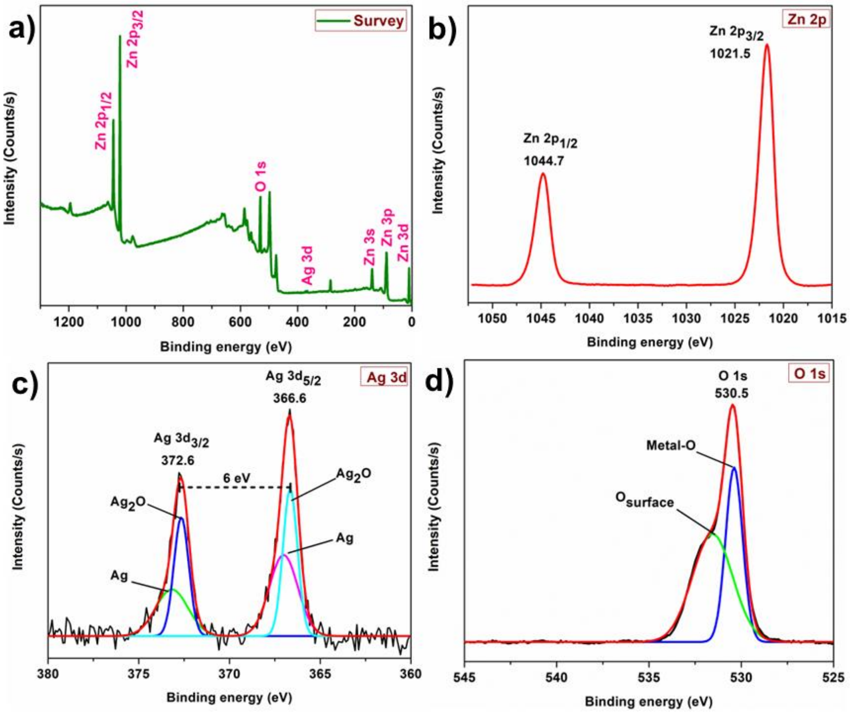

Fig. 5.10: a) XPS survey spectrum for $Ag/Ag_2O/ZnO$ (**2a**) nanocomposite, b-d) corresponding XPS spectra of Zn 2p, Ag 3d and O 1s, respectively.

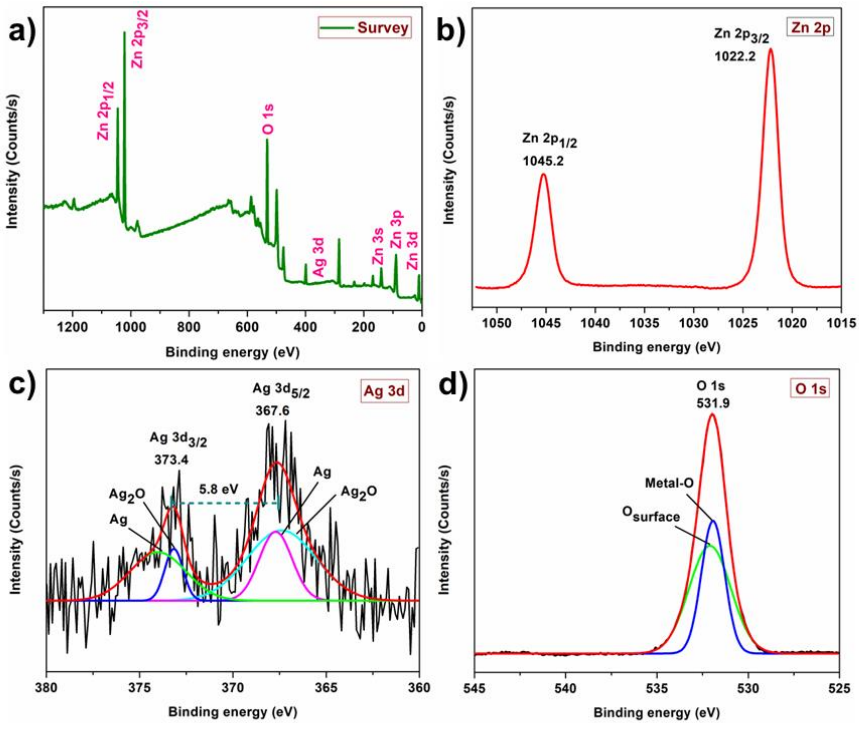

Fig. 5.11: a) XPS survey spectrum for Ag/Ag_2O/ZnO (**2b**) nanocomposite, b-d) corresponding XPS spectra of Zn 2p, Ag 3d and O 1s, respectively.

5.2.1.9. UV-Visible Diffuse Reflectance Spectroscopy analysis (DRS)

The UV-Vis diffuse reflectance spectra of Ag doped nanomaterials **2a** and **2b** were analyzed (**Fig. 5.12a-b**), which displayed typical sharp absorption edges of ZnO nanomaterial around 380 nm in both cases. The red shift of 10 nm absorption peak relative to other ZnO nanostructures [54, 32] indicated enhanced photoactivity of Ag decorated ZnO nanomaterials in visible region. Both the samples (**2a** & **2b**) evidenced integration of Ag-nanoparticles in ZnO nanomaterials by showing wide absorption covering visible region (400-800 nm) due to surface plasmon resonance effect of Ag nanoparticles [54, 55, 56]. The UV-DRS spectra of **2a** & **2b** identified their light absorbing capabilities in UV and visible range, which facilitated them to be great choices for photocatalytic reactions.

The correlation of absorption efficiency (**α**) and photon energy (hν) provided the optical bandgaps (Eg) of **2a** and **2b** nanomaterials, which were calculated using Tauc equation (**1B.2**) **(Chapter 1B, sub-unit 1B.3.9)** [53]:

$$(\alpha h\nu)^2 = A(h\nu - Eg) \qquad \textbf{Equation (1B.2)}$$

The calculated bandgap energy for **2a** was found to be somewhat smaller (1.386 eV) than that of **2b** (1.429 eV) (**Fig. 5.12c-d**). The significant decrease in the bandgap energies for both the materials as compared to pure ZnO nanocrystals (3.3 eV) [32, 53] was believed to be due to the integration of Ag particles (as Ag metal and Ag_2O) in the **2a** and **2b** nanomaterials.

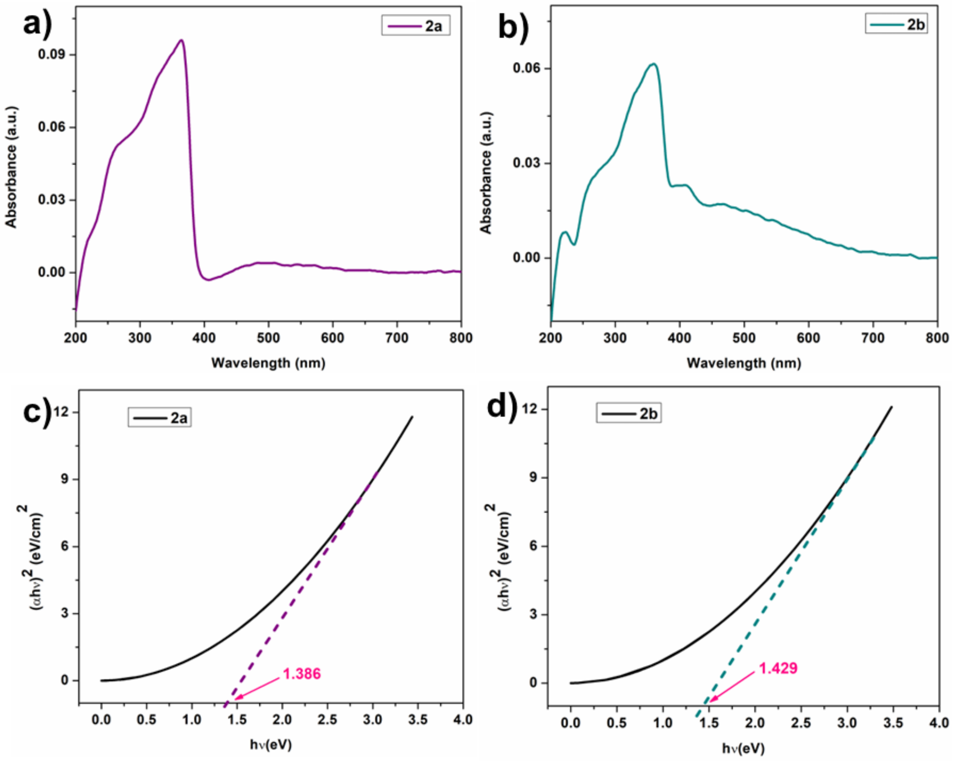

Fig. 5.12: UV-DRS spectra of a) **2a**, b) **2b**; Tauc plots of c) **2a**, d) **2b** nanomaterials.

5.2.2. Catalytic study

The photocatalytic efficiency of $Ag/Ag_2O/ZnO$ nanocomposites (**2a** and **2b**) were studied for degradation of a model cationic organic dye, methylene blue (MB) and its mixtures with other dyes, namely, methyl orange (MO) and crystal violet (CV) under sunlight. The optimization for various reaction conditions was done using the model dye. The degradation processes under all the reaction conditions were carried out using UV-visible spectroscopy. Initially, the photocatalytic performances of the catalysts were checked under direct sunlight for 10 ppm MB dye solutions at pH 10 by taking 15 mg of **2a** catalyst, where 97.19% dye decomposition was observed from the UV-Vis spectra within 80 min of exposure to sun (**Fig. 5.13a**). Similarly, 15 mg of **2b** catalyst also effectively degraded 95.61% dye from the basic MB solution in 80 min of reaction time (**Fig. 5.14a**).

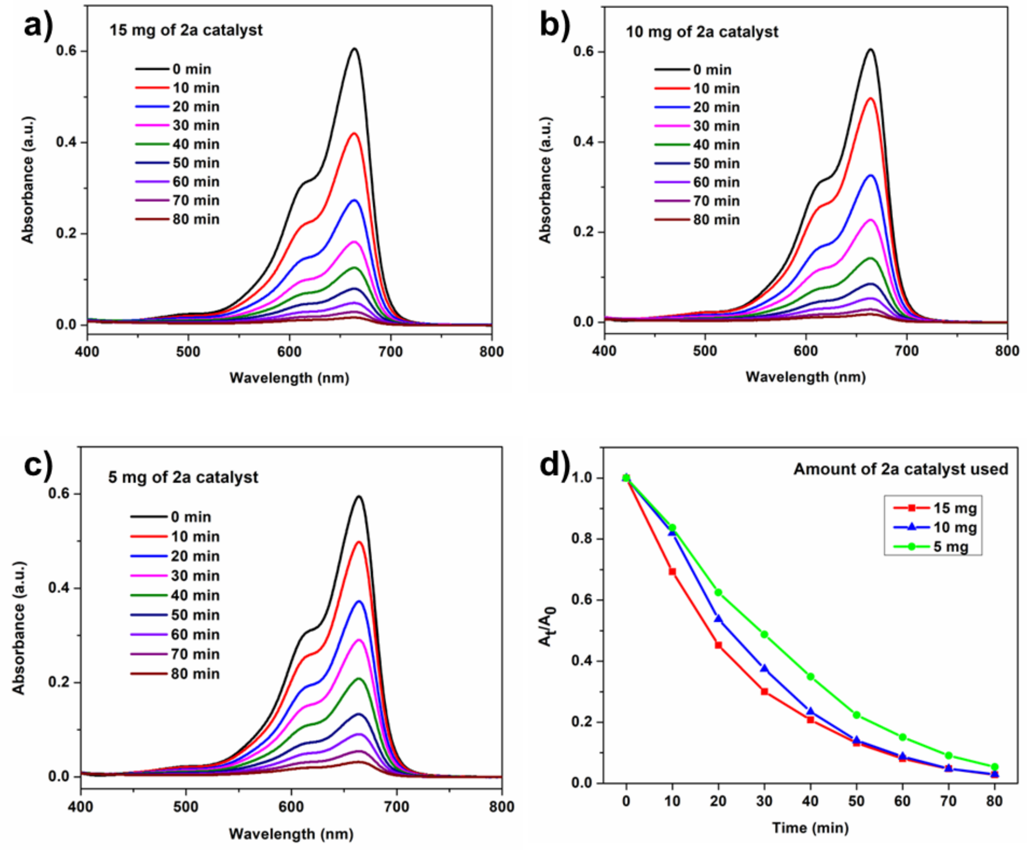

Fig. 5.13: UV-Visible spectra for degradation of MB dye at pH 10 under sunlight using a) 15 mg of **2a**, b) 10 mg of **2a**, c) 5 mg of **2a**, d) effect of varying catalyst amounts of **2a** on the degradation of MB at pH 10.

Upon varying the catalyst amount under the same reaction conditions, 10 mg and 5 mg of **2a** caused 97.02% and 94.62% dye degradation, respectively, (**Fig. 5.13b-c**), while 10 mg and 5 mg of **2b** caused 91.37% and 82.11% dye degradation, respectively, (**Fig. 5.14b-c**) within 80 min of reaction. It was observed from these results that the catalyst **2a** possessed better photocatalytic activity than **2b**, as expected from the lower band gap values of **2a** (1.386 eV) than **2b** (1.429 eV), although the surface area value of **2b** was somewhat greater than that of **2a**. Therefore, 15 mg of **2a** was considered as optimized catalyst amount for further degradation reactions. The degradation rate (%) of MB was calculated according to the following **Equation 6.1**:

$$\text{Degradation rate (\%)} = \{(A_0 - A_t)/A_0\} \times 100 \qquad \textbf{(Equation 6.1)}$$

where, A_0 is the initial absorbance of MB solution after attaining the adsorption-desorption equilibrium and A_t is the absorbance of MB solution at any given time ‘t’ during the reaction.

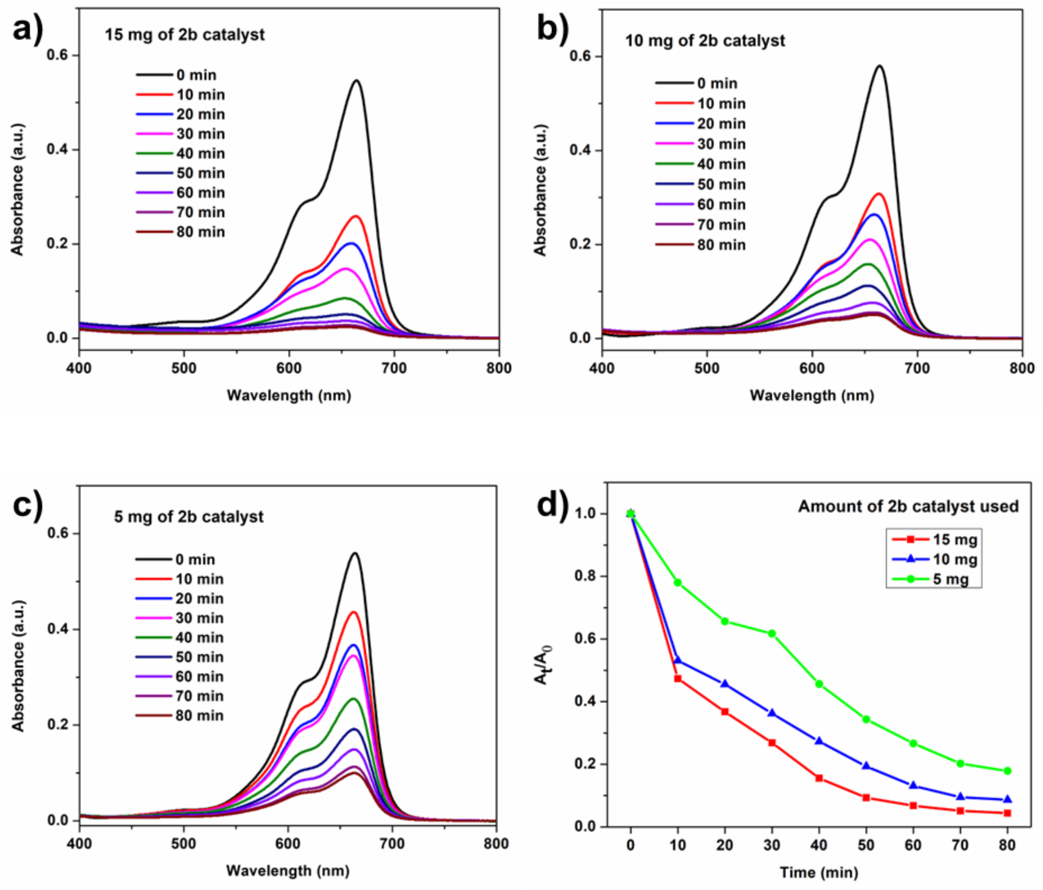

Fig. 5.14: UV-Visible spectra for degradation of MB dye at pH 10 under sunlight using a) 15 mg of **2b**, b) 10 mg of **2b**, c) 5 mg of **2b**, d) effect of varying catalyst amounts of **2b** on the degradation of MB at pH 10.

The order of MB dye degradation by 15 mg of **2a** at pH 10 was attained from the linear fit regression plot of ln (A_t/A_0) versus reaction time (**Fig. 5.15a**). From this plot, the correlation coefficient value was found to be R^2= 0.995, which indicated that the photocatalytic degradation of MB followed the pseudo-first order kinetics. From the slope of this plot, the rate constant k was found to be -0.0443 min^{-1}, which represented the rate constant for MB dye degradation by 15 mg of **2a** catalyst at pH 10. Similarly, the linear fit regression plot for MB degradation by 15 mg of **2b** catalyst at pH 10 produced rate constant k= -0.0393 min^{-1} and correlation coefficient R^2= 0.977, again pointing towards the pseudo-first order kinetics (**Fig. 5.15b**).

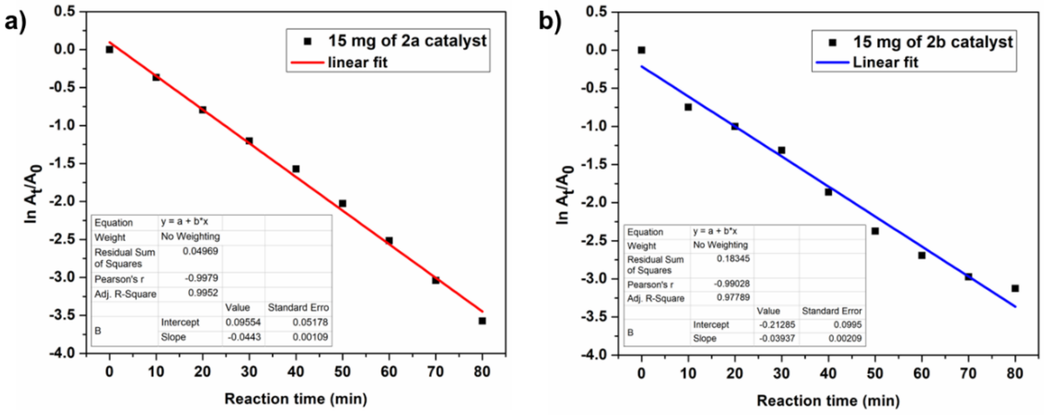

Fig. 5.15: Pseudo-first order linear fit regression plots for decomposition of MB dye at pH 10 under sunlight using a) 15 mg of **2a**, b) 15 mg of **2b** catalyst.

The effect of pH on the degradation of MB dye by 15 mg of **2a** catalyst under sunlight was studied (**Fig. 5.16a**). It was found that the catalyst exhibited excellent degradation performance under basic conditions (pH 10), degrading 97.19% MB dye within 80 min of reaction time. At neutral pH, a decent degradation of 70.3% dye was obtained. The catalyst performed comparatively poorly under acidic conditions (pH 4), where only 57.83% dye was degraded in 80 min. These observations for the degradation of cationic MB dye at varied pH values indicated that at higher pH, on the surface of the nanocomposite, greater number of negatively charged sites might be available for adsorption of the MB dye as compared to lower pH values of the solutions for non-competitive photo degradation reactions. The degradation rate of MB was also studied in a mixed dye solution with methyl orange (MO). In case of mixed dye MB+MO, better degradation rate was seen for MO than for MB at all the pH studied, where complete degradation of MO occurred within 20-60 min under basic to acidic conditions, respectively. In this mixture, the degradation of MB was still poor at acidic or neutral pH (**Fig. 5.17a-c**). This observation reflects that the overall degradation of any dye over the nanocomposites may depend on various factors including pH of the solution, competitive degradation reactions in the mixtures of dyes etc. Thus, the better degradation of MO in the mixture could be attributed to competitive consumption of MO involving oxidizing species as well as photo-reactive azo group (N=N) of the MO, whereas the less reactive -CH_3 group present in MB forced it to combat photodegradation [57-60]. Again, when MB was mixed with another cationic dye crystal violet (CV), competitive degradation of either of the dyes was not observed and both the dyes followed similar degradation pattern to show almost complete decomposition at basic pH and poor degradation under acidic environment (**Fig. 5.17d-f**).

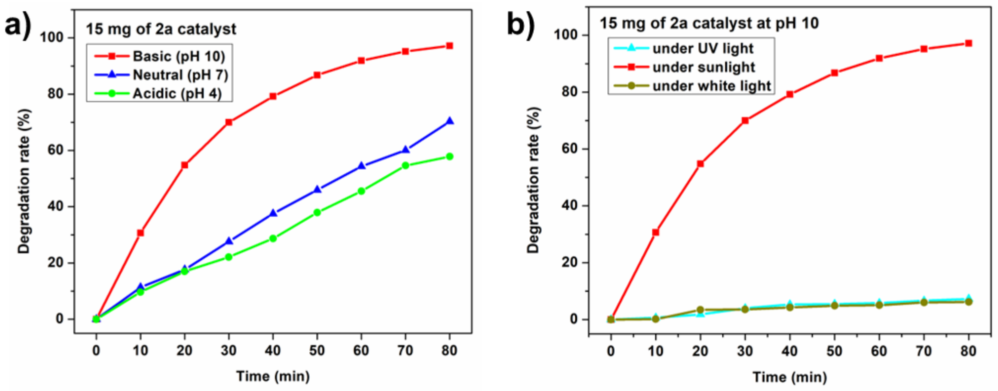

Fig. 5.16: a) Effect of varying pH on the degradation rates (%) of MB by 15 mg of **2a** catalyst, b) effect of varying light source on the degradation rates (%) of MB by 15 mg of **2a** catalyst.

Again, the outcomes of using different light sources on the degradation of MB dye by 15 mg of **2a** catalyst were also investigated (**Fig. 5.16b**). Using both UV light (11 W) and white light (7 W) resulted in extremely poor degradation rate (%) of MB dye i.e. 7.28% and 6.18%, respectively, as compared to that in presence of sunlight under similar reaction conditions.

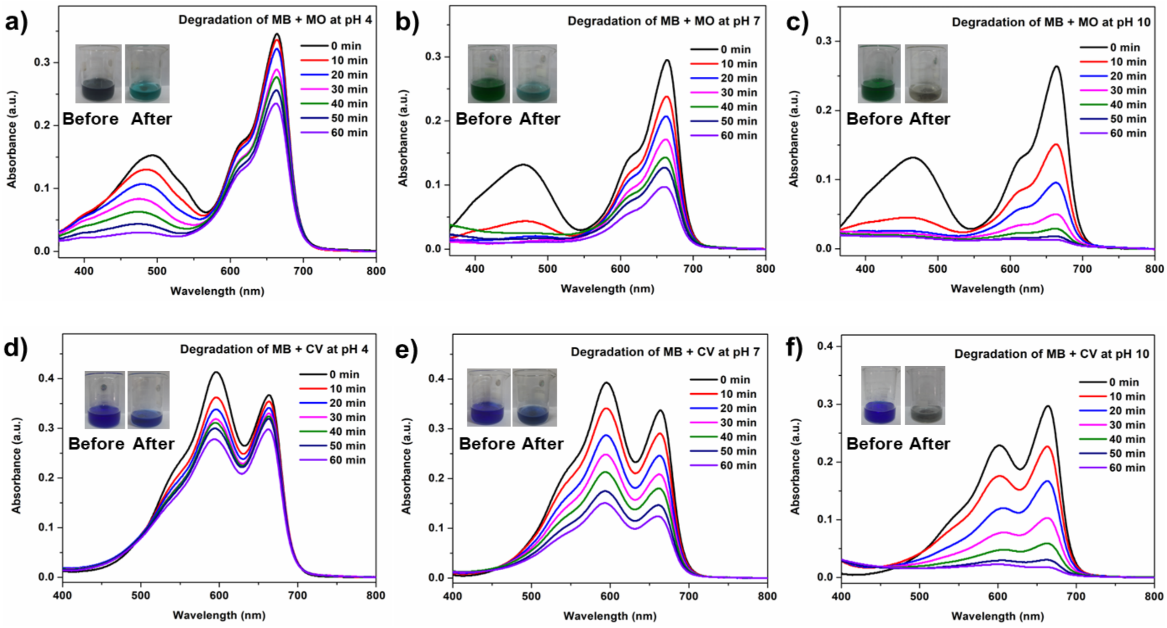

Fig. 5.17: UV-Vis spectra for degradation of a-c) mixture of MB+MO dye, d-f) mixture of MB+CV dye, at varying pH by 15 mg of **2a** catalyst, under sunlight.

5.2.2.1. Detection of active species in dye degradation process

In general, during the photocatalytic degradation of organic pollutants, the material having semiconductor properties, absorbs photon energy and produces photogenerated electrons (e^-) in the valence band (VB), which are promoted to conduction band (CB) of the semiconductor. The resultant free electrons (e^-) and holes (h^+) in the CB and VB, respectively, can associate with the dissolved O_2 molecules or H_2O to produce superoxide radical anion ($^{\bullet}O_2^-$) and hydroxyl radical ($^{\bullet}OH$), that act as primary reactive species in the photocatalytic degradation of organic pollutants [61]. To find out the reactive species involved in the sunlight driven dye degradation, a radical scavenger in 1mM concentration was added to the MB solution containing 15 mg of **2a** catalyst at pH 10. The scavengers $AgNO_3$, Na_2-EDTA, isopropanol and *p*-benzoquinone were used for e^-, h^+, $^{\bullet}OH$ and $^{\bullet}O_2^-$ species, respectively. It was noticed from **Fig. 5.18** that after addition of the scavengers to the dye solution, the degradation rate of MB was reduced as compared to that in absence of the scavengers. The least degradation (21.21%) of MB was observed in case of *p*-benzoquinone scavenger, which indicated that the degradation process was mostly governed by $^{\bullet}O_2^-$ species. Moreover, in presence of e^- scavenging $AgNO_3$, 66.56% degradation was observed, while addition of Na_2-EDTA caused 77.17% degradation. However, 87.37% dye was degraded when h^+ scavenging isopropanol was added. By observing the extent of degradation even after the addition of scavengers, it could be assumed that both the electrons and superoxide radical anions were the dominant reactive species in the degradation mechanism of MB dye under visible light.

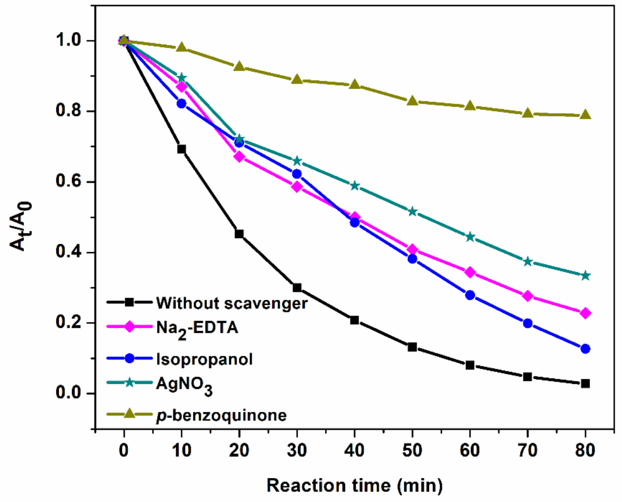

Fig. 5.18: Degradation rate of MB by **2a** catalyst after the addition of various radical scavengers.

5.2.2.2. Plausible mechanism for dye degradation

Scheme 5.2 illustrated a plausible mechanism for the degradation of MB dye under sunlight by Ag/Ag_2O/ZnO nanocomposites. Under visible light, ZnO does not produce photoelectrons and holes due to its wide band gap energy of around 3.3 eV, resulting in the low photocatalytic efficiency for the degradation of organic pollutants [45, 33]. But in case of the Ag based nanocomposites of ZnO, the NPs of Ag components could absorb the visible light energy owing to surface plasmon resonance effect (SPR) effect and induce photogenerated electrons and holes. These electrons could migrate from the Ag based components to the CB of ZnO component through the heterojunction interface, leaving behind holes in the VB of Ag component. It could be expected that with lower band gap of 1.2 eV, the Ag_2O component could also generate the electron/hole pairs easily and these electrons could also migrate to the CB of ZnO phase [62]. The photogenerated electrons in the CB of ZnO and Ag_2O could react with the dissolved oxygen to produce superoxide radical anions $^\bullet O_2^-$ and the holes present on the VB of Ag_2O could react with H_2O to produce hydroxyl radicals $^\bullet OH$. The resultant reactive oxygen species played a major role in the photocatalytic degradation of the organic dye. From previous reports also, it was noticed that the fabrication of Ag/Ag_2O/ZnO nano heterocomposites by adding Ag and Ag_2O to ZnO could significantly improve the photocatalytic behaviour of ZnO under visible light [33, 32].

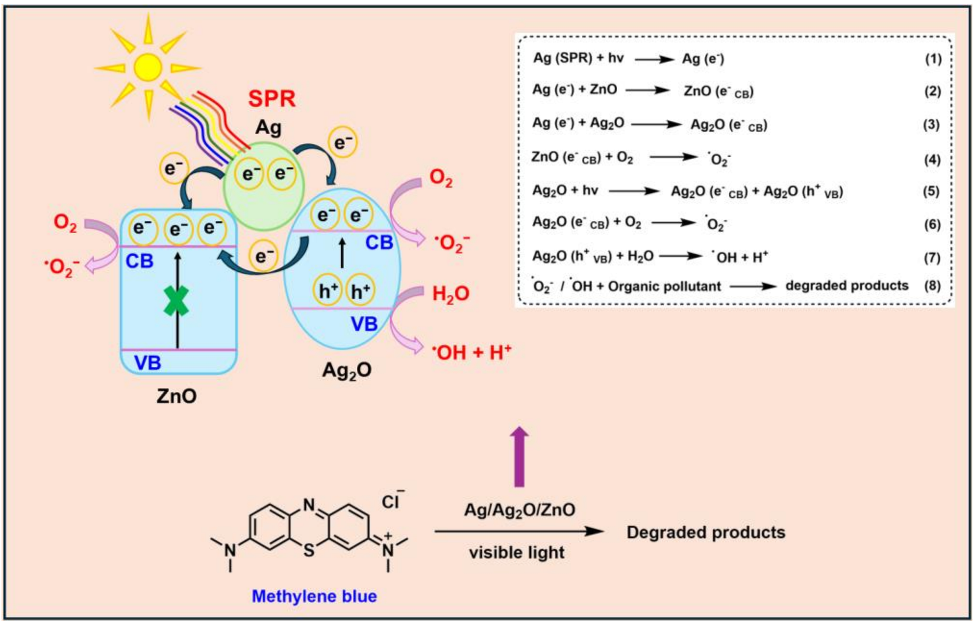

Scheme 5.2: Plausible mechanism for MB dye degradation under sunlight by Ag/Ag_2O/ZnO nanocomposites.

5.2.3. Recyclability study of the catalyst

The reusability of **2a** catalyst was checked in the photocatalytic degradation of MB dye under basic condition (pH 10) for 4 consecutive cycles, after getting excellent results in the first run. In the recovery process, the catalyst was first collected from the degraded dye solution by centrifugation, and then washed repeatedly with distilled water to remove any traces of the dye from it. It was also washed thoroughly with ethanol till neutralization. After reactivating the catalyst by drying it in a vacuum oven for 24 h, its composition was checked via FTIR and PXRD techniques. As the integrity of the recovered catalyst was established, it was used in another cycle of catalytic degradation of the MB under same conditions. Minimal loss in the catalyst activity was observed from the % degradation in 2nd run, while the 4th cycle displayed a decent result as compared to the first one (**Fig. 5.19a**).

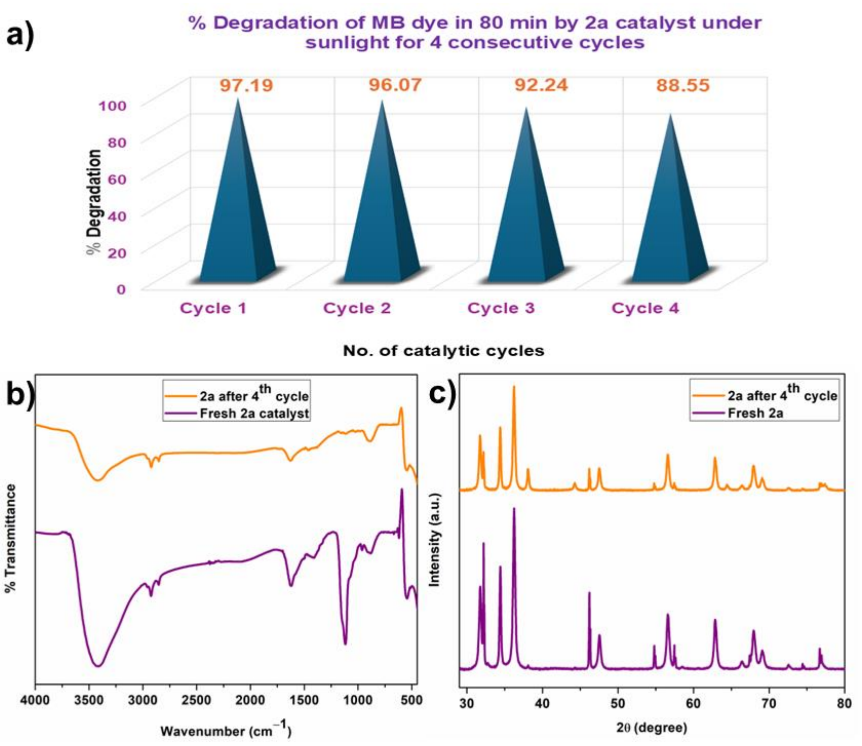

Fig. 5.19: a) Bar diagram revealing **2a** catalyst recyclability for MB degradation in 80 min under sunlight, b) FTIR spectrum of recovered **2a** catalyst as compared to the fresh one, c) PXRD pattern of recovered **2a** catalyst as compared to the fresh one.

The FTIR spectrum of the recovered catalyst showed the presence of most peaks as shown by the fresh catalyst, although their intensities were somewhat decreased in the former (**Fig. 5.19b**). The PXRD pattern of the recovered catalyst exhibited no shift in 2θ values of the diffractions, but the intensities of the peaks were altered as compared to the PXRD pattern of the fresh catalyst (**Fig. 5.19c**). EDX as well as elemental mapping showed that the constituent elements of **2a** were still intact in the recovered material (**Fig. 5.20**).

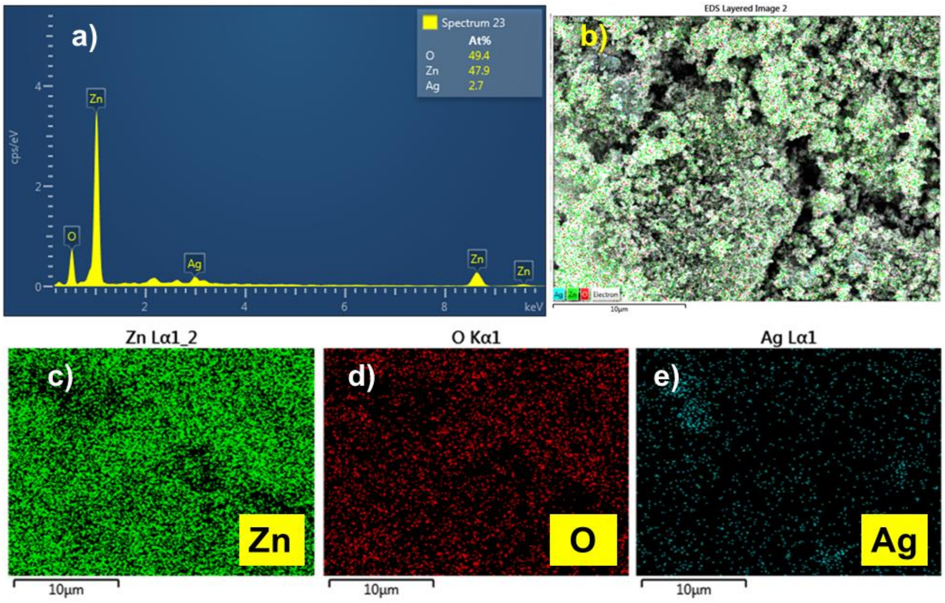

Fig. 5.20: a) EDX image of recovered **2a** (atomic% of elements in inset), b-e) elemental mapping images of all the constituent atoms of recovered **2a** material.

5.3. Summary

In summary, two heterostructured nanocomposites of Ag/Ag_2O/ZnO were developed as efficient photo responsive catalysts for degradation of model dye MB and its mixtures with anionic/cationic dyes under optimized conditions in visible region. Both the nanocomposites were fabricated with tuned morphologies assisted by two organic salts of chloride anion with varied sizes of the organic cations in aqueous solution. EDX and XPS analyses verified the elemental composition of the prepared nanocomposites. Surface morphologies, as observed in SEM images of the two nanocomposites, displayed different sizes and shapes of the crystallite nanoparticles. The calculated band gap energies of two nanocomposites reflected efficient modification in the semiconductor properties of ZnO in visible region. The photocatalysts showed good reusability with 88.6% degradation efficiency of the MB dye after 4 cycles. Thus, the results expressed significant enhancement of the photo-efficiency of Ag integrated ZnO heterostructures for degradation of organic pollutants in water.

5.4. Experimental section

5.4.1. Synthetic procedure for $Ag/Ag_2O/ZnO$ nanocomposites

The synthesis of Ag integrated ZnO nanocomposites (**2a** & **2b**) were prepared by following reaction **Scheme 5.1** from the reaction of $Zn(NO_3)_2.6H_2O$ and 10% $AgNO_3$ salts with sodium hydroxide in aqueous solution of two Brønsted acidic organic salts of piperazinium and imidazolium cations, respectively, which worked as stabilizing agents during nanoparticle formations. Initially, the two organic salts, namely 1,4-disulfopiperazine-1,4-diium chloride ([DSPZ].2Cl]), a dicationic organic salt and 1,3-disulfoimidazolium chloride ([MDSIM]Cl), a monocationic room temperature ionic liquid, were prepared as per the standard literature procedures [28, 29]. Then, to synthesize the **2a** composite, 10 mmol of the [DSPZ].2Cl was added to a mixture of aqueous solution of 10 mmol $Zn(NO_3)_2.6H_2O$ and 1 mmol $AgNO_3$ salts contained in a 100 mL round-bottom flask at 90 °C temperature, which was allowed to stir for 30 min. To that, 10 mL of 2 M NaOH solution was added dropwise, which immediately resulted in the formation of white-coloured precipitate within the flask and was left to continuously stir for 2 h at 90 °C. After that the reaction was stopped, cooled down to ambient temperature and filtered to get the residue. The residue was then washed extensively with distilled water as well as ethanol and dried in a vacuum oven at 80 °C for 12 h. Then, the powdered residue was subjected to heating in a muffle furnace at 300 °C for 2 h, which produced the $Ag/Ag_2O/ZnO$ (**2a**) as a pale lavender coloured powder. Similarly, 10 mmol of the [MDSIM]Cl was used instead of [DSPZ].2Cl, keeping the rest of the procedure same, to synthesize another composite of $Ag/Ag_2O/ZnO$ (**2b)** as a pale peach coloured powder.

5.4.2. General procedure for decomposition of organic dyes using $Ag/Ag_2O/ZnO$ nanocomposites

At first, 10 ppm aqueous solution of MB dye was prepared. For experiments that involved the degradation of MB dye, 25 mL of a 10 ppm aqueous dye solution was taken in a 50 ml beaker, to which the synthesized nanocomposite (**2a** or **2b**) was added. The suspension was allowed to stir continuously for 45 min to establish the adsorption-desorption equilibrium. After obtaining the adsorption-desorption equilibrium, the reaction mixture was exposed to direct and continuous sunlight for the photocatalytic decomposition of the dye molecules to occur. 1 mL aliquot was collected after every 10 min intervals, which was centrifuged to separate the catalyst from the dye solution for further use. Up on diluting the aliquots with 1:2 ratio, the UV-visible spectra of these reaction mixtures were recorded to get the absorbance values, from which the progress of the degradation processes was monitored. For the degradation of binary dye solution, 12.5 mL of a 10 ppm aqueous MB solution and 12.5 mL a 10 ppm aqueous MO/CV solution were mixed to get a 25 mL solution of mixture of dyes. The rest of the degradation processes was exactly like that stated above.

5.4.3. Spectral data of the parent organic salts

1,4-disulfopiperazine-1,4-diium chloride ([DSPZ].2Cl]): White solid, FT-IR (KBr) ν cm^{-1}: 3415, 3250, 3009, 1641, 1559, 1442, 1318, 1174, 1064, 941, 864, 741 and 583; ^{1}H NMR: (DMSO-d_6, 400 MHz): δ 9.32 (s, 2H), 6.58 (s, 2H), 3.29 (s, 8H); ^{13}C NMR: (DMSO-d_6), 100 MHz): δ 87.35.

1,3-disulfoimidazolium chloride ([MDSIM]Cl): Yellow viscous liquid, FT-IR (KBr) ν cm^{-1}: 3415, 3168, 2927, 2735, 1628, 1428, 1192, 1054, 754, 583; ^{1}H NMR: (DMSO-d_6, 400 MHz): δ 13.86 (s, 2H), 7.43 (s, 2H), 2.50 (s, 3H); ^{13}C NMR: (DMSO-d_6), 100 MHz): δ 144.62, 119.18, 11.54.

5.4.4. Spectra of parent organic salts

a) FT-IR spectrum of 1,4-disulfopiperazine-1,4-diium chloride ([DSPZ].2Cl])

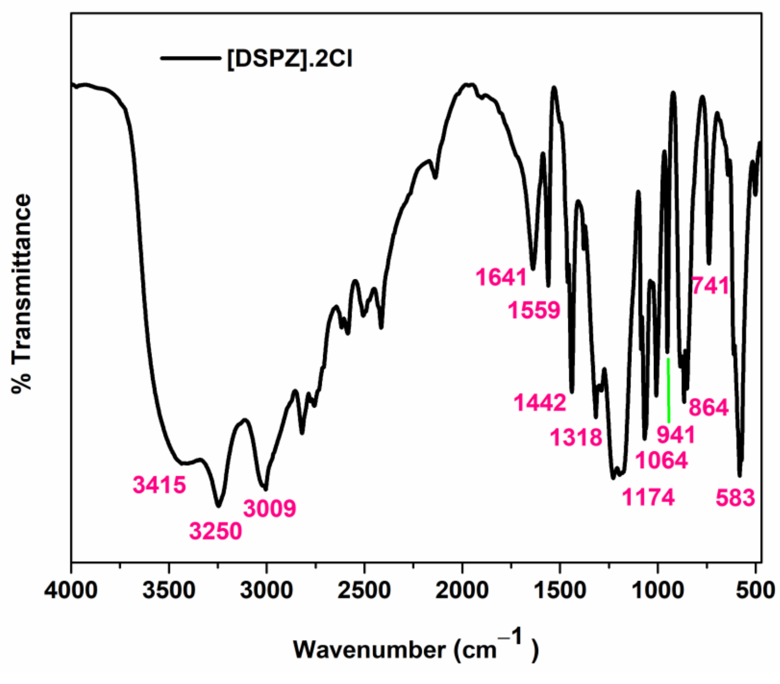

b) ^{1}H NMR of 1,4-disulfopiperazine-1,4-diium chloride ([DSPZ].2Cl])

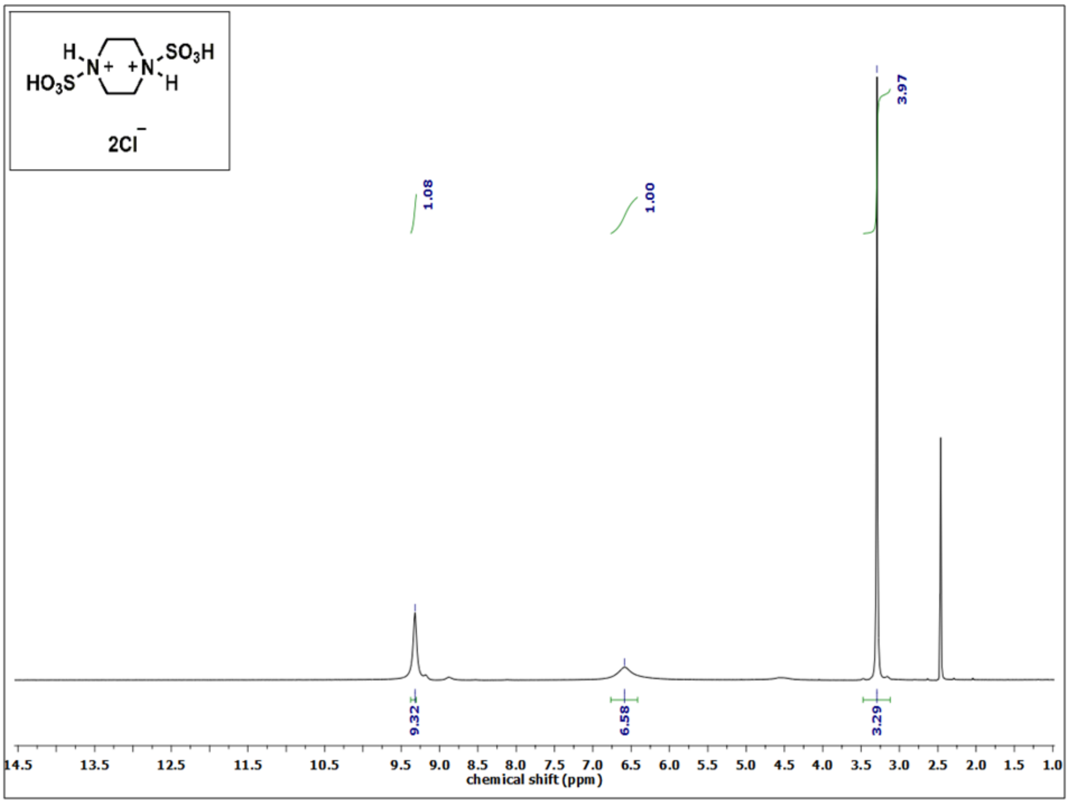

c) ^{13}C NMR of 1,4-disulfopiperazine-1,4-diium chloride ([DSPZ].2Cl])

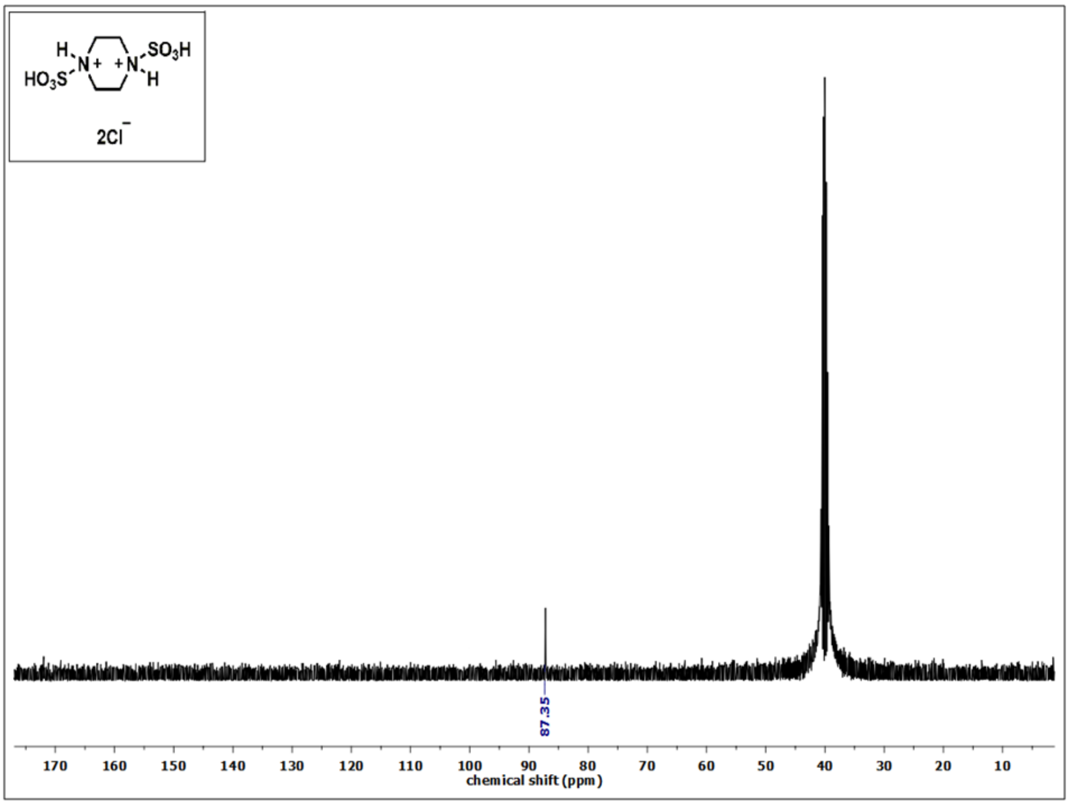

d) FT-IR spectrum of 1,3-disulfoimidazolium chloride ([MDSIM]Cl)

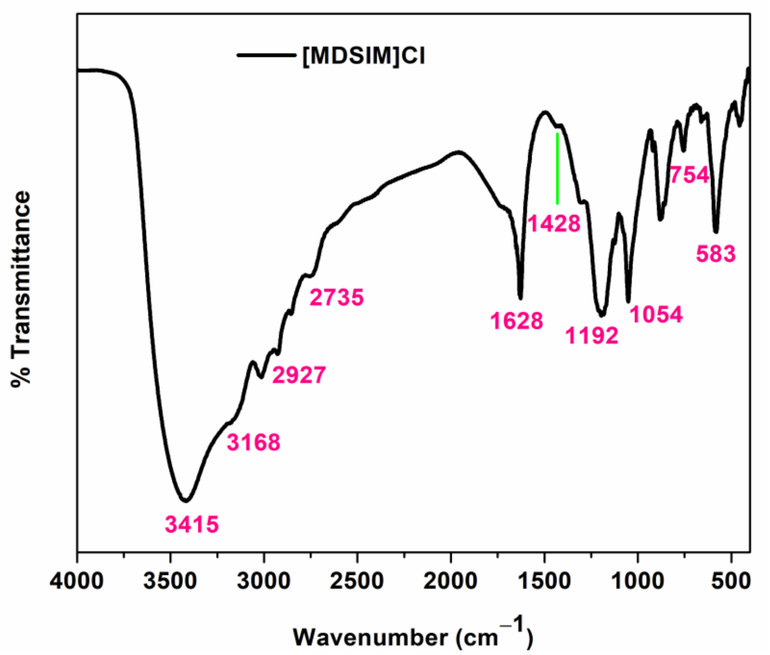

e) ^{1}H NMR of 1,3-disulfoimidazolium chloride ([MDSIM]Cl)

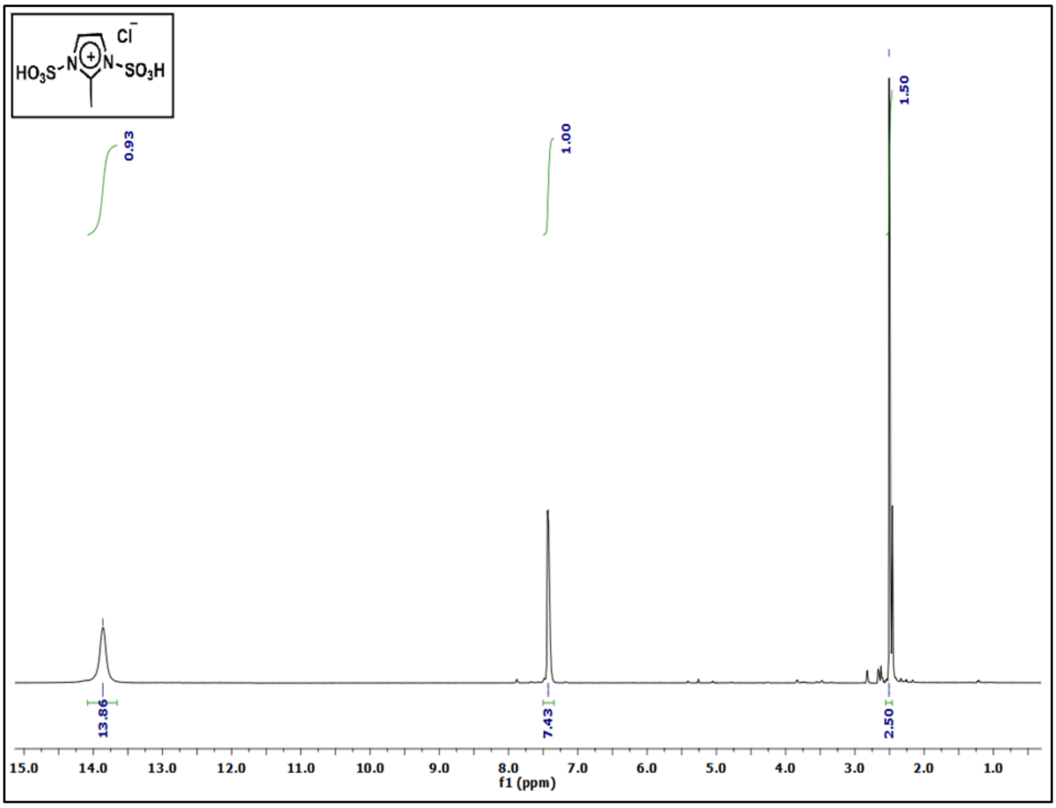

f) ^{13}C NMR of 1,3-disulfoimidazolium chloride ([MDSIM]Cl)

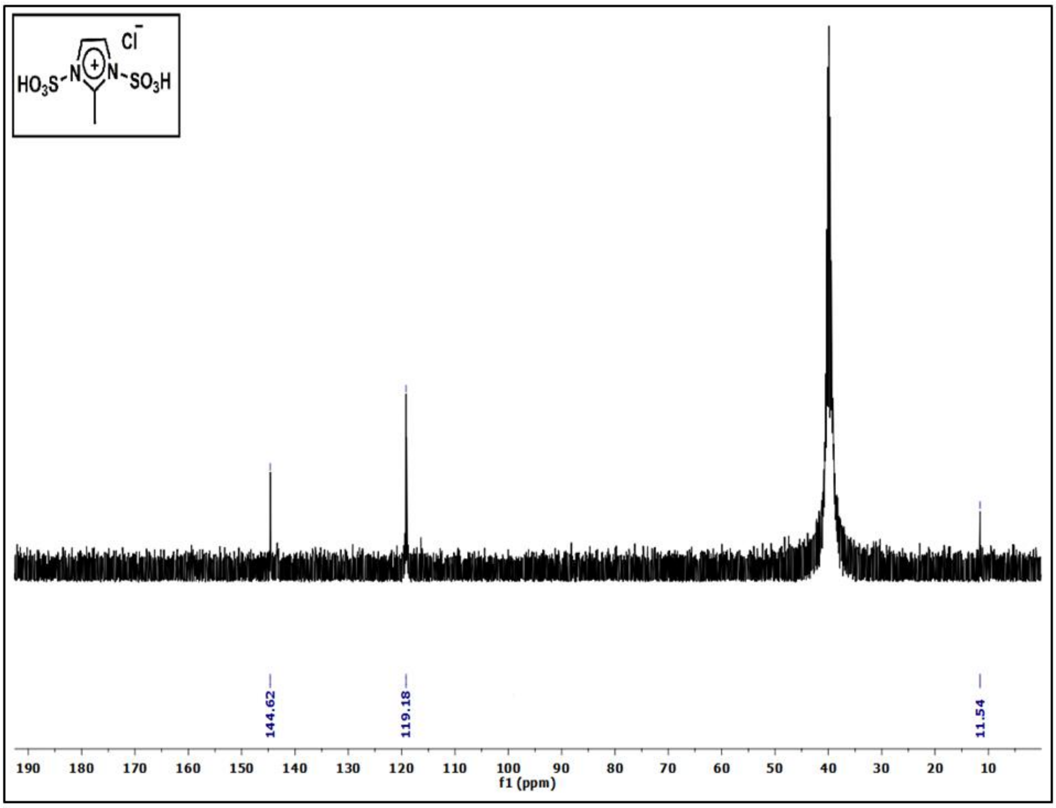

5.5. Bibliography

[1] Geim, A. K. and Grigorieva, I. V. Van der Waals heterostructures. *Nature*, 499(7459):419-425, 2013.

[2] Jariwala, D., Sangwan, V. K., Lauhon, L. J., Marks, T. J., and Hersam, M. C. Emerging device applications for semiconducting two-dimensional transition metal dichalcogenides. *ACS Nano*, 8(2):1102-1120, 2014.

[3] Zhang, Y., Zhu, X., and Zhang, Y. Exploring heterostructured upconversion nanoparticles: from rational engineering to diverse applications. *ACS Nano*, 15(3):3709-3735, 2021.

[4] Jamkhande, P. G., Ghule, N. W., Bamer, A. H., and Kalaskar, M. G. Metal nanoparticles synthesis: An overview on methods of preparation, advantages and disadvantages, and applications. *Journal of Drug Delivery Science and Technology*, 53:101174, 2019.

[5] Bordiwala, R. V. Green synthesis and applications of metal nanoparticles.-A review article. *Results in Chemistry*, 5:100832, 2023.

[6] Phuruangrat, A., Siri, S., Wadbua, P., Thongtem, S., and Thongtem, T. Microwave-assisted synthesis, photocatalysis and antibacterial activity of Ag nanoparticles supported on ZnO flowers. *Journal of Physics and Chemistry of Solids*, 126:170-177, 2019.

[7] Satdeve, N. S., Ugwekar, R. P., and Bhanvase, B. A. Ultrasound assisted preparation and characterization of Ag supported on ZnO nanoparticles for visible light degradation of methylene blue dye. *Journal of Molecular Liquids*, 291:111313, 2019.

[8] Farag, H. K., El-Shamy, A. M., Sherif, E. M., and Zein El Abedin, S. Sonochemical synthesis of nanostructured ZnO/Ag composites in an ionic liquid. *Zeitschrift für Physikalische Chemie*, 230(12):1733-1744, 2016.

[9] Zhao, S., Zhang, Y., Zhou, Y., Zhang, C., Fang, J., and Sheng, X. Ionic liquid-assisted photochemical synthesis of ZnO/Ag_2O heterostructures with enhanced visible light photocatalytic activity. *Applied Surface Science*, 410:344-353, 2017.

[10] Dule, M., Biswas, M., Biswas, Y., and Mandal, T. K. Redox-active poly (ionic liquid)-engineered Ag nanoparticle-decorated ZnO nanoflower heterostructure: A reusable composite catalyst for photopolymerization into high-molecular-weight polymers. *Polymer*, 133:223-231, 2017.

[11] Ta, Q. T. H., Park, S., and Noh, J. S. Ag nanowire/ZnO nanobush hybrid structures for improved photocatalytic activity. *Journal of Colloid and Interface Science*, 505:437-444, 2017.

[12] Gao, S., Zhang, H., Wang, X., Deng, R., Sun, D., and Zheng, G. ZnO-based hollow microspheres: Biopolymer-assisted assemblies from ZnO nanorods. *The Journal of Physical Chemistry B*, 110(32):15847-15852, 2006.

[13] Han, X. G., He, H. Z., Kuang, Q., Zhou, X., Zhang, X. H., Xu, T., Xie, Z. X., and Zheng, L.S. Controlling morphologies and tuning the related properties of nano/microstructured ZnO crystallites. *The Journal of Physical Chemistry C*, 113(2):584-589,2009.

[14] Yıldırım, Ö. A., Unalan, H. E., and Durucan, C. Highly efficient room temperature synthesis of silver-doped zinc oxide (ZnO: Ag) nanoparticles: Structural, optical, and photocatalytic properties. *Journal of the American Ceramic Society*, 96(3):766-773, 2013.

[15] Ansari, S. A., Ansari, S. G., Foaud, H., and Cho, M. H. Facile and sustainable synthesis of carbon-doped ZnO nanostructures towards the superior visible light photocatalytic performance. *New Journal of Chemistry*, 41(17):9314-9320, 2017.

[16] Patil, S. S., Mali, M. G., Tamboli, M. S., Patil, D. R., Kulkarni, M. V., Yoon, H., Kim, H., Al-Deyab, S. S., Yoon, S. S., Kolekar, S. S., and Kale, B. B. Green approach for hierarchical nanostructured Ag-ZnO and their photocatalytic performance under sunlight. *Catalysis Today*, 260:126-134, 2016.

[17] Umar, A., Rahman, M. M., Kim, S. H., and Hahn, Y. B. Zinc oxide nanonail based chemical sensor for hydrazine detection. *Chemical Communications*, (2):166-168, 2008.

[18] Sugiura, E., Furukawa, M., Tateishi, I., Katsumata, H., and Kaneco, S. Development of Ag/Ag_2O/ZnO photocatalyst and their photocatalytic activity towards dibutyl phthalate decomposition in water. *Journal of the Air & Waste Management Association*, 72(10):1137-1152, 2022.

[19] Pawinrat, P., Mekasuwandumrong, O., and Panpranot, J. Synthesis of Au-ZnO and Pt-ZnO nanocomposites by one-step flame spray pyrolysis and its application for photocatalytic degradation of dyes. *Catalysis Communications*, 10(10):1380-1385, 2009.

[20] Muñoz-Fernandez, L., Sierra-Fernández, A., Milošević, O., and Rabanal, M. E. Solvothermal synthesis of Ag/ZnO and Pt/ZnO nanocomposites and comparison of their photocatalytic behaviors on dyes degradation. *Advanced Powder Technology*, 27(3):983-993, 2016.

[21] Yu, C., Yang, K., Xie, Y., Fan, Q., Jimmy, C. Y., Shu, Q., and Wang, C. Novel hollow Pt-ZnO nanocomposite microspheres with hierarchical structure and enhanced photocatalytic activity and stability. *Nanoscale*, 5(5):2142-2151, 2013.

[22] Liu, Y., Li, P., Xue, R., and Fan, X. Research on catalytic performance and mechanism of Ag_2O/ZnO heterostructure under UV and visible light. *Chemical Physics Letters*, 746:137301, 2020.

[23] Mousavi-Kouhi, S. M., Beyk-Khormizi, A., Amiri, M. S., Mashreghi, M., and Yazdi, M. E. T. Silver-zinc oxide nanocomposite: from synthesis to antimicrobial and anticancer properties. *Ceramics International*, 47(15):21490-21497, 2021.

[24] Wegner, S. and Janiak, C. Metal nanoparticles in ionic liquids. *Topics in Current Chemistry*, 375:1-32, 2017.

[25] Redel, E., Thomann, R., and Janiak, C. Use of ionic liquids (ILs) for the IL-anion size-dependent formation of Cr, Mo and W nanoparticles from metal carbonyl $M(CO)_6$ precursors. *Chemical Communications*, (15):1789-1791, 2008.

[26] Zhao, S., Zhang, Y., Zhou, Y., Zhang, C., Fang, J., and Sheng, X. Ionic liquid-assisted photochemical synthesis of ZnO/Ag_2O heterostructures with enhanced visible light photocatalytic activity. *Applied Surface Science*, 410:344-353, 2017.

[27] Farag, H. K., El-Shamy, A. M., Sherif, E. M., and Zein El Abedin, S. Sonochemical synthesis of nanostructured ZnO/Ag composites in an ionic liquid. *Zeitschrift für Physikalische Chemie*, 230(12):1733-1744, 2016.

[28] Koodehi, T. G., Shirini, F., and Goli-Jolodar, O. Preparation, characterization and application of 1, 4-disulfopiperazine-1, 4-diium chloride ([Piper-$(SO_3H)_2$].2Cl) as an efficient dicationic ionic catalyst for the N-Boc protection of amines. *Journal of the Iranian Chemical Society*, 14:443-456, 2017.

[29] Saikia, S. and Borah, R. 2-Methyl-1, 3-disulfoimidazolium polyoxometalate hybrid catalytic systems as equivalent safer alternatives to concentrated sulfuric acid in nitration of aromatic compounds. *Applied Organometallic Chemistry*, 33(10):5146, 2019.

[30] Tkaczyk, A., Mitrowska, K., and Posyniak, A. Synthetic organic dyes as contaminants of the aquatic environment and their implications for ecosystems: A review. *Science of the Total Environment*, 717:137222, 2020.

[31] Khan, W. U., Ahmed, S., Dhoble, Y., and Madhav, S. A critical review of hazardous waste generation from textile industries and associated ecological impacts. *Journal of the Indian Chemical Society*, 100(1):100829, 2023.

[32] Umukoro, E. H., Peleyeju, M. G., Ngila, J. C., and Arotiba, O. A. Photocatalytic degradation of acid blue 74 in water using Ag-Ag_2O-ZnO nanostuctures anchored on graphene oxide. *Solid State Sciences*, 51:66-73, 2016.

[33] Ding, W., Zhao, L., Yan, H., Wang, X., Liu, X., Zhang, X., Huang, X., Hang, R., Wang, Y., Yao, X., and Tang, B. Bovine serum albumin assisted synthesis of $Ag/Ag_2O/ZnO$ photocatalyst with enhanced photocatalytic activity under visible light. *Colloids and Surfaces A: Physicochemical and Engineering Aspects*, 568:131-140, 2019.

[34] Bechambi, O., Chalbi, M., Najjar, W., and Sayadi, S. Photocatalytic activity of ZnO doped with Ag on the degradation of endocrine disrupting under UV

irradiation and the investigation of its antibacterial activity. *Applied Surface Science*, 347:414-420, 2015.

[35] Yang, Z., Deng, C., Ding, Y., Luo, H., Yin, J., Jiang, Y., Zhang, P., and Jiang, Y. Eco-friendly and effective strategy to synthesize ZnO/Ag_2O heterostructures and its excellent photocatalytic property under visible light. *Journal of Solid-State Chemistry*, 268:83-93, 2018.

[36] Abbasi, M. Design, preparation and characterization of a new ionic liquid, 1, 3-disulfonic acid benzimidazolium chloride, as an efficient and recyclable catalyst for the synthesis of tetrahydropyridine under solvent-free conditions. *RSC Advances*, 5(83):67405-67411, 2015.

[37] Rahman, M. M., Khan, S. B., Jamal, A., Faisal, M., and Asiri, A. M. Fabrication of highly sensitive acetone sensor based on sonochemically prepared as-grown Ag_2O nanostructures. *Chemical Engineering Journal*, 192:122-128, 2012.

[38] Xiong, G., Pal, U., Serrano, J. G., Ucer, K. B., and Williams, R. T. Photoluminesence and FTIR study of ZnO nanoparticles: The impurity and defect perspective. *Physica Status Solidi C*, 3(10):3577-3581, 2006.

[39] Vivek, C., Balraj, B., and Thangavel, S. Structural, optical and electrical behavior of ZnO@ Ag core–shell nanocomposite synthesized via novel plasmon-green mediated approach. *Journal of Materials Science: Materials in Electronics*, 30(12):11220-11230, 2019.

[40] Changlin, Y. U., Kai, Y. A. N. G., Qing, S. H. U., Jimmy, C. Y., Fangfang, C. A. O., and Xin, L. I. Preparation of WO_3/ZnO composite photocatalyst and its photocatalytic performance. *Chinese Journal of Catalysis*, 32(3-4):555-565, 2011.

[41] Musa, I., Qamhieh, N., and Mahmoud, S. T. Synthesis and length dependent photoluminescence property of zinc oxide nanorods. *Results in Physics*, 7:3552-3556, 2017.

[42] Xia, H. and Yang, G. Facile synthesis of inorganic nanoparticles by a precipitation method in molten ε-caprolactam solvent. *Journal of Materials Chemistry*, 22(35):18664-18670, 2012.

[43] Li, H., Liu, E. T., Chan, F. Y., Lu, Z., and Chen, R. Fabrication of ordered flower-like ZnO nanostructures by a microwave and ultrasonic combined technique and their enhanced photocatalytic activity. *Materials Letters*, 65(23-24):3440-3443, 2011.

[44] Zhan, T., Ding, G., Cao, W., Li, J., She, X., and Teng, H. Amperometric sensing of catechol by using a nanocomposite prepared from Ag/Ag_2O nanoparticles and N, S-doped carbon quantum dots. *Microchimica Acta*, 186:1-9, 2019.

[45] Liang, Y., Guo, N., Li, L., Li, R., Ji, G., and Gan, S. Facile synthesis of Ag/ZnO micro-flowers and their improved ultraviolet and visible light photocatalytic activity. *New Journal of Chemistry*, 40(2):1587-1594, 2016.

[46] Al-Musawi, T. J., Rajiv, P., Mengelizadeh, N., Arghavan, F. S., and Balarak, D. Photocatalytic efficiency of $CuNiFe_2O_4$ nanoparticles loaded on multi-walled carbon nanotubes as a novel photocatalyst for ampicillin degradation. *Journal of Molecular Liquids*, 337:116470, 2021.

[47] Pandey, P., Parra, M. R., Haque, F. Z., and Kurchania, R. Effects of annealing temperature optimization on the efficiency of ZnO nanoparticles photoanode based dye sensitized solar cells. *Journal of Materials Science: Materials in Electronics*, 28:1537-1545, 2017.

[48] Mosquera, E., Rojas-Michea, C., Morel, M., Gracia, F., Fuenzalida, V., and Zárate, R. A. Zinc oxide nanoparticles with incorporated silver: Structural, morphological, optical and vibrational properties. *Applied Surface Science*, 347:561-568, 2015.

[49] Filippov, S., Wang, X. J., Devika, M., Koteeswara Reddy, N., Tu, C. W., Chen, W. M., and Buyanova, I. A. Effects of Ni-coating on ZnO nanowires: A Raman scattering study. *Journal of Applied Physics*, 113(21), 2013.

[50] Nakamoto, K. *Infrared and Raman Spectra of Inorganic and Coordination Compounds, Part B: Applications in Coordination, Organometallic, and Bioinorganic Chemistry*. John Wiley & Sons, New Jersey, USA, 6th edition, 2009.

[51] Karagoz, S., Kiremitler, N. B., Sarp, G., Pekdemir, S., Salem, S., Goksu, A. G., Onses, M. S., Sozdutmaz, I., Sahmetlioglu, E., Ozkara, E. S., and Ceylan, A. Antibacterial, antiviral, and self-cleaning mats with sensing capabilities based on electrospun nanofibers decorated with ZnO nanorods and Ag nanoparticles for protective clothing applications. *ACS Applied Materials & Interfaces*, 13(4):5678-5690, 2021.

[52] Zielińska, A., Kowalska, E., Sobczak, J. W., Łącka, I., Gazda, M., Ohtani, B., Hupka, J., and Zaleska, A. Silver-doped TiO_2 prepared by microemulsion method: Surface properties, bio-and photoactivity. *Separation and Purification Technology*, 72(3):309-318, 2010.

[53] Liu, Y., Li, P., Xue, R., and Fan, X. Research on catalytic performance and mechanism of Ag_2O/ZnO heterostructure under UV and visible light. *Chemical Physics Letters*, 746:137301, 2020.

[54] Han, Z., Ren, L., Cui, Z., Chen, C., Pan, H., and Chen, J. Ag/ZnO flower heterostructures as a visible light driven photocatalyst via surface plasmon resonance. *Applied Catalysis B: Environmental*, 126:298-305, 2012.

[55] Haghighi, A., Haghighi, M., Shabani, M., and Fard, S. G. Oxygen-rich bismuth oxybromide nanosheets coupled with Ag_2O as Z-scheme nano-heterostructured plasmonic photocatalyst: Solar light-activated photodegradation of dye pollutants. *Journal of Hazardous Materials*, 408:124406, 2021.

[56] Wang, D., Xue, G., Zhen, Y., Fu, F., and Li, D. Monodispersed Ag nanoparticles loaded on the surface of spherical Bi_2WO_6 nanoarchitectures with enhanced photocatalytic activities. *Journal of Materials Chemistry*, 22(11):4751-4758, 2012.

[57] Nezamzadeh-Ejhieh, A. and Karimi-Shamsabadi, M. Comparison of photocatalytic efficiency of supported CuO onto micro and nano particles of zeolite X in photodecolorization of Methylene blue and Methyl orange aqueous mixture. *Applied Catalysis A: General*, 477:83-92, 2014.

[58] Liu, S., Liu, C., Wang, W., Cheng, B., and Yu, J. Unique photocatalytic oxidation reactivity and selectivity of TiO_2-graphene nanocomposites, *Nanoscale,* 4:3193–3200, 2012.

[59] Huo, R., Kuang, Y., Zhao, Z., Zhang, F., and Xu, S. Enhanced photocatalytic performances of hierarchical ZnO/$ZnAl_2O_4$ microsphere derived from layered double hydroxide precursor spray-dried microsphere. *Journal of Colloid and Interface Science*, 407:17-21, 2013.

[60] Hameed, A., Gombac, V., Montini, T., Graziani, M., and Fornasiero, P. Synthesis, characterization and photocatalytic activity of NiO-Bi_2O_3 nanocomposites. *Chemical Physics Letters*, 472(4-6):212-216, 2009.

[61] Liu, H., Zhong, L., Govindaraju, S., and Yun, K. ZnO rod decorated with Ag nanoparticles for enhanced photocatalytic degradation of methylene blue. *Journal of Physics and Chemistry of Solids*, 129:46-53, 2019.

[62] Fresno, F., Portela, R., Suárez, S., and Coronado, J. M. Photocatalytic materials: Recent achievements and near future trends. *Journal of Materials Chemistry A*, 2(9):2863-2884, 2014.